Simulations of Wave Propagation and Wave–wave Interactions in the Solar Corona and Solar Wind

Master's thesis
University of Turku
Physics
2021
B.Sc. Seve Nyberg
Examiners:
Prof. Rami Vainio
Dr. Alexandr Afanasiev

According to the University of Turku quality control specifications, this text has been checked with Turnitin Originality Check.

UNIVERSITY OF TURKU
Department of Physics and Astronomy

Nyberg, Seve Simulations of Wave Propagation and Wave–wave Interactions in the Solar Corona and Solar Wind

Master's thesis, 61 p., appendix, 3 p.
Physics
June 2021

Several numerical methods, notably upwind schemes, Lax–Wendroff schemes, and a semi-Lagrangian scheme, are investigated in order to find suitable models to simulate Alfvén wave transport and evolution. The tools are assessed by comparing the simulation results of open magnetic field line settings to analytical solutions of the simulation problems.

The most promising model found is a semi-Lagrangian scheme, due to its accuracy and computational efficiency, but it is currently limited to time invariant wave velocities. As an option to the semi-Lagrangian scheme the conservative Lax–Wendroff scheme was found to reproduce analytically solved results with a good accuracy.

The semi-Lagrangian scheme is used to investigate wave–wave interactions in a closed magnetic field line setting, a coronal loop. The coronal loop setting is heavily simplified in order to observe the effects of wave–wave interactions on the spectra. The wave–wave interactions discussed are of the smallest order approximation level: three-wave interactions comprising of Alfvén waves and a sound wave. The three-wave interactions can clearly be seen altering the wave energy density spectra injected. The results may have implications in particle transport, and as such are interesting results to be investigated more.

The simulation methods used are deemed sufficient, albeit improvements can be made, and as such are capable of simulating Alfvén wave spectra that are an important part of simulating particle acceleration in the solar corona.

Keywords: Alfvén waves, wave propagation, wave–wave interactions, numerical methods, simulations, Solar corona, Solar wind

TURUN YLIOPISTO
Fysiikan ja tähtitieteen laitos

Nyberg, Seve Aaltojen etenemisen ja aalto–aalto-vuorovaikutusten simulointi koronassa ja aurinkotuulessa

Pro Gradu, 61 s., liitteet, 3 s.
Fysiikka
Kesäkuu 2021

Tutkielmassa etsitään tarkkaa ja tehokasta numeerista menetelmää Alfvénin aaltojen etenemisen ja vuorovaikutusten mallintamiseen. Etenemisen mallinukseen kehitettiin ylätuulimenetelmiä, Lax–Wendroff-menetelmiä ja puolilagrangelainen menetelmä. Menetelmien soveltuvuutta arvioidaan vertailemalla simulaatiotuloksia analyyttisiin tuloksiin koronan ja aurinkotuulen avoimella magneettikenttäviivalla.

Lupaavimmaksi simulaatiomalliksi osoittautuu puolilagrangelainen menetelmä, jota kuitenkin rajoittaa vaatimus aaltojen nopeuksien aikariippumattomuudesta. Vaihtoehtoinen lupaava menetelmä on konservatiivinen Lax–Wendroff-menetelmä, joka toistaa kohtuullisen tarkasti analyyttisia tuloksia ja sallii ajasta riippuvat aaltonopeudet.

Aalto–aalto-vuorovaikutuksia tutkitaan koronan suljetulla magneetikenttäviivalla käyttäen puolilagrangelaista menetelmää. Plasman ominaisuuksia kenttäviivaa ympäröivässä koronan silmukassa yksinkertaistetaan, jotta aaltospektrien muutosten tiedetään johtuvan aalto–aalto-vuorovaikutuksista. Aalto–aalto-vuorovaikutukset käsitellään matalimman kertaluokan approksimaatioina, kolmiaaltovuorovaikutuksina, joissa kaksi Alfvénin aaltoa ja ääniaalto vuorovaikuttavat keskenään. Kolmiaaltovuorovaikutusten huomataan selvästi muuttavan aaltojen energiatiheysspektrejä. Tuloksilla on vaikutusta ainakin varattujen hiukkasten kuljetukseen koronan silmukoissa. Tämän osalta jatkotutkimukset ovat tarpeen.

Tutkitut simulaatiomenetelmät ovat riittäviä simuloimaan Alfvénin aaltojen spektrejä. Aaltojen spektrit ovat olennaisen tärkeitä mm. koronan hiukkaskiihdytyksen mallinnuksessa, johon tulevissa tutkimuksissa myös keskitytään.

Asiasanat: Alfvénin aallot, aaltojen eteneminen, aalto–aalto-vuorovaikutukset, numeeriset menetelmät, simulaatiot, Auringon korona, aurinkotuuli

Contents

1 Introduction

Alfvén waves are incompressible transverse hydromagnetic waves, that propagate parallel to the magnetic field lines. Alfvén wave transport and evolution are important processes in the solar wind and the solar corona. Particle transport and coronal heating are both dependent on the wave populations of the coronal and interplanetary plasma, leading to the importance of understanding wave transport and evolution.

The aim of this thesis is to create tools to investigate Alfvén wave transport and wave–wave interactions to better understand the underlying physics of these systems. The results of this investigation can be used, for example, in shock wave simulations, where the Alfvén wave spectra hold a role in particle acceleration. Examples of these kinds of simulations can be found in [1–4].

We expect through this investigation to find sufficient simulation models to simulate Alfvén wave transport, without significant numerical errors. In addition to the simulation models, tools to optimize and improve corresponding simulations are investigated.

We will first dive into the underlying theory to give the reader a brief look into the history and background of the research of Alfvén waves and their interactions with other constituents of plasma, after which we will be going through the models investigated and results attained from them.

Understanding the wave propagation and wave–wave interactions requires knowledge of the environment around. The Sun is in a key part in producing the features of the interplanetary space environment. The solar wind and its plasma wave modes are also a key factor in shaping solar energetic particle events. Understanding the mechanisms of these components is essential to understanding wave-particle and wave-wave interactions.

Plasma is a quasi-neutral gas whose behavior is governed by electromagnetic

fields. A gas with an ionization degree as small as 0.1 % can already look like plasma and an ionization degree of 1 % leads to an almost perfect conductivity [5]. Sufficient heat and ionizing radiation are the mechanisms that create and uphold the plasma state of matter.

The interplanetary space is a complex system of charged particles, radiation, electromagnetic fields, plasma streams and waves, all fueled by the Sun. Understanding the processes powering the Sun and the effects the Sun has on our surrounding has taken giant leaps during the last century. One of the first major advancements were the measurements of intense magnetic fields in sunspots by Hale in 1908, showing that varying magnetic fields on the surface of the Sun might be key to solar activity. [5, 6]

The Sun has a complex structure, with many layers with different roles and processes. The visible parts of the surface of the Sun are called the photosphere and chromosphere. Right above the photosphere and the chromosphere lies the *corona*, which we will be focusing on more in this text. The corona is significantly hotter at about 10^6 K, compared to the Sun's surface at about 5800 K, and hosts many dynamic phenomena that result in particle acceleration and the solar wind. The corona has an intricate and ever-moving structure that is governed by solar magnetism. In a coordinate system that has no electric field pointing perpendicular to the magnetic field, plasma and energetic particles flow mainly along the magnetic field lines. Generally, such coordinate systems can exist only locally. In the case of the solar corona, however, the perpendicular electric field is minimized in the coordinate system rotating with the Sun, and that allows one to trace the global evolution of coronal plasma as a one-dimensional expansion inside flux tubes defined by the magnetic field lines. [5, 7]

In the 1950s a theory of a continuous outflow of particles from the Sun began to emerge, notably pioneered by Biermann [8, 9] and Alfvén [10]. Alfvén noted that the

outflow must be magnetized plasma. In 1958, Parker [11] derived an approximate solution to the geometry of the flow. In an inertial frame the plasma flow is close to radial, but in the frame rotating with the Sun the flow is in a form of a spiral, dubbed the *Parker spiral*. The Parker spiral is a simplified, yet still important concept in current view of the solar wind and the magnetic field frozen into it. According to Koskinen [5], there are two main types of solar wind, a fast solar wind and a slow solar wind. Fast wind is generally accepted to be originated from large coronal holes at high solar latitudes and the slow solar wind from smaller structures at lower latitudes.

The transportation of the effects of solar activity on the surface of the Sun to the interplanetary space is in part done by the magnetic field of the solar wind, the *interplanetary magnetic field* (IMF) [5]. The magnetic field is frozen into the plasma as it propagates outwards from the Sun and expands, forming the Parker spiral.

Plasma can support several different wave modes, ranging from oscillations of particles to fluctuations of the electromagnetic field. We will be reviewing only the sound waves and Alfvén waves of the plasma, since we are investigating the propagation and interactions of these waves.

As in other media, sound waves are pressure fluctuations inside the system. Sound waves are primarily measured by pressure or particle density fluctuations, ΔP or Δn. The plasma in these waves fluctuates along the magnetic field lines, but do not cause magnetic disturbances in the system. The sound speed is defined as

$$c_S = \sqrt{\frac{\gamma k_B T}{m}} = \sqrt{\frac{\gamma P}{\rho}} = \frac{\omega}{k}, \tag{1}$$

where γ is the adiabatic index, k_B is the Boltzmann constant, T the temperature of the all of the constituents of the system (electrons and ions), m the average mass of a molecule ($m \approx m_i/2$, where m_i is the mass of an ion, due to the relatively small mass of the electron), P the pressure of the medium, ρ the mass density of

the medium, ω the wave angular frequency, and k the wavenumber. [5, 12]

In 1942, Hannes Alfvén [13] drew attention to electromagnetic-hydrodynamic waves in conducting liquids. Disturbing the liquid caused the charge carriers to induce a magnetic field, causing mechanical forces on the carriers themselves. This result was extrapolated to the Sun's magnetic field, where solar matter was a good conductor, and later dubbed *Alfvén waves*.

Alfvén waves are transverse magnetic field fluctuations that propagate parallel to the magnetic field lines. Differing from sound waves, these waves are incompressible. Intuitively Alfvén waves can be derived from considering the magnetic field lines as strings with tension. Perturbing the string causes a propagating perturbation along the string, the Alfvén wave. The Alfvén speed in the direction of the magnetic field is defined as

$$v_A = \sqrt{\frac{B^2}{\mu_0 \rho_m}} = \frac{\omega}{k}, \tag{2}$$

where B is the magnetic field magnitude, μ_0 the vacuum permeability, and ρ_m the mass density of the plasma. The plasma's movement and the magnetic disturbances caused by the waves are perpendicular to the magnetic field, and related to each other as

$$\Delta \boldsymbol{B} = -\frac{\Delta \boldsymbol{V}}{\pm v_A} B_0, \tag{3}$$

where $\Delta \boldsymbol{B}$ is the magnetic field vector of the fluctuation, $\Delta \boldsymbol{V}$ the velocity vector of the fluctuating medium, and B_0 the background magnetic field. The signs in the denominator correspond to the propagation direction of the wave either parallel (+) or anti-parallel (–) to the field. [5, 12]

Another key process in the evolution of the waves are wave–wave interactions. In this thesis we will be using three-wave interactions between two Alfvén waves and a sound wave to describe the wave–wave interactions at the smallest order approximation level. This *weak turbulence approximation* will be discussed more in section 3.1.

2 Alfvén Wave Propagation in the Solar Wind

2.1 Theoretical Background

There are many models for wave propagation, and the simplest one of them is *Wentzel–Kramers–Brillouin* (WKB) transport. WKB is a method to find approximate solutions to differential equations, originally used in quantum mechanics to solve the Schrödinger equation. It has been found to be a useful tool in calculating wave propagation in inhomogeneous media [5]. The condition for the WKB method to be applicable in wave transport calculation is that the wavelength of the wave packets being investigated is significantly shorter than the gradient scale lengths of the background media. WKB transport is a sufficient model to describe Alfvén wave transport in simple settings, as in [14–19], and can be found to imitate observed data of the solar corona and wave spectra (discussed in [20–23]). WKB theory is equivalent to a semi-classical description of wave packets propagating as quasi-particles in the coronal medium, obeying a Hamiltonian of form

$$H(\boldsymbol{r}, \boldsymbol{p}) = \hbar\omega(\boldsymbol{r}, \boldsymbol{p}/\hbar),$$

where $\boldsymbol{p} = \hbar\boldsymbol{k}$ and

$$\omega = \omega(\boldsymbol{r}, \boldsymbol{k})$$

is the dispersion relation of the wave.

Ng et al. [14] derive an equation for the evolution of properties of radially outwards propagating Alfvén waves, which is the basis for our simulation arithmetic. The equation derivation will be also discussed here to connect the underlying theory to the simulation.

Ng et al. start from the wave kinetic equation described by Dewar [24], Barnes [25], and Stix [26]

$$\frac{\partial \mathcal{N}_\sigma}{\partial t} + \frac{\partial \omega}{\partial \boldsymbol{k}} \cdot \frac{\partial \mathcal{N}_\sigma}{\partial \boldsymbol{r}} - \frac{\partial \omega}{\partial \boldsymbol{r}} \cdot \frac{\partial \mathcal{N}_\sigma}{\partial \boldsymbol{k}} = \gamma_\sigma \mathcal{N}_\sigma \tag{4}$$

where $\mathcal{N}_\sigma$ is the wave action density, defined as $\hbar$ times the number density of plasmons in the six-dimensional phase space $(\boldsymbol{r}, \boldsymbol{k})$, ω is the angular frequency, $\boldsymbol{k}$ is the wave vector, $\boldsymbol{r}$ is the position vector, and $\gamma_\sigma \mathcal{N}_\sigma$ the source term, where γ_σ is the net wave growth rate. If we consider radially outward propagating waves, we can write the wave action density in spherical coordinates (r, θ, ϕ) as

$$\mathcal{N}_\sigma(\boldsymbol{k}, \boldsymbol{r}, t) = \frac{N_\sigma(k, r, t)}{k^2 \sin\theta_k} \frac{\delta(\theta_k)}{2\pi} \tag{5}$$

where N_σ is the plasmon density distribution per unit wavenumber, k the wave number, and (k, θ_k, ϕ_k) are the spherical coordinates in $\boldsymbol{k}$-space with the polar axis aligned along $\boldsymbol{r}$. The wave dispersion relation in the fixed frame,

$$\omega = kV_{\sigma f} = k(V_{sw} + V_\sigma) = k(V_{sw} + v_A), \tag{6}$$

where ω is the wave angular frequency, $V_{\sigma f}$ the wave velocity in the fixed frame and V_σ the wave velocity in the plasma frame, V_{sw} the solar wind speed, and v_A the Alfvén velocity, is time-independent, leading us to

$$\frac{\mathrm{d}\omega}{\mathrm{d}t} = \frac{\partial\omega}{\partial t} = 0.$$

The fixed frame and plasma-frame wave speeds, $V_{\sigma f}$ and V_σ, are defined as

$$V_{\sigma f} = V_{sw} + v_A \tag{7}$$

$$V_\sigma = v_A \tag{8}$$

for Alfvén waves propagating outwards from the Sun. Choosing an analytically solvable case to compare simulation data with theory, we choose a constant solar wind speed, which gives a r^{-2} dependence for the density, and a radially diverging magnetic field, where the magnetic field magnitude is also proportional to the inverse square of the distance. Using this information we get

$$v_A = \frac{B}{\sqrt{\mu_0 \rho}} = \frac{a}{r} \tag{9}$$

$$V_{sw} = v, \tag{10}$$

where a and v are constant simulation parameters. This approximation is valid in the inner part of the solar wind.

To observe the evolution of the wave quanta we use a spectral magnetic intensity, I^σ, defined as

$$\langle(\delta \boldsymbol{B})^2\rangle = A \int I^\sigma(k)\mathrm{d}k, \tag{11}$$

where A is a normalization factor set to unity in this work. To draw a relation between the wave action density, N_σ, and the spectral magnetic intensity I^σ, we start from the definition of N_σ:

$$N_\sigma(k) = \frac{E(k)}{\omega'},$$

where $E(k)$ is the spectral energy density and ω' the wave frequency in the plasma rest frame. The spectral energy density, $E(k)$ is defined as

$$E(k) = \frac{I^\sigma(k)}{\mu_0},$$

where μ_0 is the vacuum permeability. Combining the previous two equations we get

$$\omega' N_\sigma(k) = \frac{I^\sigma(k)}{\mu_0}.$$

Adding the definitions for the fixed frame Alfvén wave frequency, ω, and plasma rest frame Alfvén wave frequency, ω',

$$\omega' = k v_A \quad \text{and}$$
$$\omega = k(V_{sw} + v_A),$$

solving for ω',

$$\omega' = \omega \frac{v_A}{V_{sw} + v_A},$$

and then combining these

$$\begin{aligned} \omega N_\sigma &\propto I^\sigma \frac{v_A}{V_{sw} + v_A} \\ \Rightarrow \omega N_\sigma &\propto I^\sigma \frac{V_{\sigma f}}{V_\sigma} \end{aligned} \tag{12}$$

we get the relation between the wave action density and the spectral magnetic intensity.

Solving for spectral magnetic intensity I^σ from the relation (12) and the time independence of the wave dispersion relation, Ng et al. derive the evolution equation for the spectral magnetic intensity of the radially outward propagating Alfvén waves (note that unlike in [14] we use the partial derivative $\frac{\partial V_{\sigma f}}{\partial r}$ instead of the total derivative $\frac{\mathrm{d}V_{\sigma f}}{\mathrm{d}r}$ inside the partial derivative of k since the partial and total derivatives are equivalent in this case as the Alfvén waves are not dispersive):

$$\frac{\partial}{\partial t}\left(\frac{V_{\sigma f}}{V_\sigma} I^\sigma\right) + \frac{1}{r^2}\frac{\partial}{\partial r}\left(r^2 \frac{V_{\sigma f}^2}{V_\sigma} I^\sigma\right) - \frac{\partial}{\partial k}\left(k \frac{\partial V_{\sigma f}}{\partial r}\frac{V_{\sigma f}}{V_\sigma} I^\sigma\right) = \gamma_\sigma \frac{V_{\sigma f}}{V_\sigma} I^\sigma, \tag{13}$$

where r is the distance from the surface of the Sun.

Equation (13) can held as the basic equation derived from the theory. The equation can be derived to an ordinary advective form or to a conservative form, where the time derivative of the density, spatial derivative of the flux quantity, and the γ_σ-term are in balance.

Equation (13) can be solved analytically when choosing a suitable simulation setting and adjusting the observed quantities a bit. The analytical solutions for this equation are solved using the method of characteristics and are explored more in section 2.2.

2.2 Numerical Methods

Several different methods of simulating wave propagation were studied in this thesis to find an accurate and flexible numerical model to simulate wave propagation in the solar corona and solar wind. The studies were conducted in systems of open magnetic

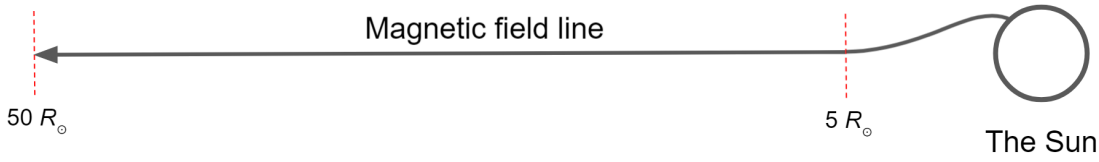

Figure 1. A depiction of the simplification of the open field lines of the magnetic field of the Sun. The magnetic field of the Sun is simplified to be radially diverging between 5 and 50 solar radii from the Sun.

field lines and closed magnetic field lines, of which the latter will be discussed more in section 3. A figure of the setting for this part of the project is shown in figure 1, where the Sun and an open magnetic field line can be seen emanating from it. The magnetic field is assumed to be radially diverging, leading to a simplified model of the Sun's magnetic field. This assumption is made to simplify the calculations substantially, without causing major issues in the interpretation of the results of these simulations.

The wave propagation equations can be studied non-conservatively (advection form) or conservatively. As the first scheme to be investigated we've chosen a non-conservative upwind scheme due to its simplicity in implementation and light computational load. Non-conservative methods studied were an upwind scheme with explicit wave growth implemented, an upwind scheme with a semi-implicit *Locally One-Dimensional* (LOD, Appendix) scheme implemented, a non-conservative Lax–Wendroff scheme (Appendix), a conservative upwind scheme, a conservative Lax-Wendroff scheme, and a semi-Lagrangian scheme. The numerical schemes and results for the non-conservative LOD upwind scheme and non-conservative Lax–Wendroff scheme have been pushed to the appendix as they are not so important for the discussion.

2.2.1 Non-conservative Flux Equations

Simplifying the wave transport equation, we denote

$$\mathcal{I}^\sigma = r^2 \frac{V_{\sigma f}^2 I^\sigma}{V_\sigma} \tag{14}$$

as a scaled magnetic intensity, which will be used to describe the magnetic intensity in our simulation setting to ease the calculations substantially. We choose to change the k-domain to a logarithmic domain of κ, where $\kappa = \ln(k/k_0)$. Multiplying equation (13) by $r^2 V_{\sigma f}$ leads to a form of

$$\frac{\partial}{\partial t}\left(r^2 \frac{V_{\sigma f}^2}{V_\sigma} I^\sigma\right) + V_{\sigma f}\frac{\partial}{\partial r}\left(r^2 \frac{V_{\sigma f}^2}{V_\sigma} I^\sigma\right) - \frac{\partial}{\partial k}\left(k \frac{\partial V_{\sigma f}}{\partial r} r^2 \frac{V_{\sigma f}^2}{V_\sigma} I^\sigma\right) = \gamma_\sigma r^2 \frac{V_{\sigma f}^2}{V_\sigma} I^\sigma,$$

and then changing to the scaled magnetic intensity $\mathcal{I}^\sigma$ results in

$$\Rightarrow \frac{\partial}{\partial t}(\mathcal{I}^\sigma) + V_{\sigma f}\frac{\partial}{\partial r}(\mathcal{I}^\sigma) - \frac{\partial}{\partial k}\left(k \frac{\partial V_{\sigma f}}{\partial r} \mathcal{I}^\sigma\right) = \gamma_\sigma \mathcal{I}^\sigma.$$

The partial derivative of k is opened and the logarithmic term κ is plugged in to result in

$$\Rightarrow \frac{\partial \mathcal{I}^\sigma}{\partial t} + V_{\sigma f}\frac{\partial \mathcal{I}^\sigma}{\partial r} - \frac{\partial V_{\sigma f}}{\partial r}\mathcal{I}^\sigma - \frac{\partial V_{\sigma f}}{\partial r}\frac{\partial \mathcal{I}^\sigma}{\partial \kappa} = \gamma_\sigma \mathcal{I}^\sigma,$$

which can be derived to an advective form of

$$\Rightarrow \frac{\partial \mathcal{I}^\sigma}{\partial t} + V_{\sigma f}\frac{\partial \mathcal{I}^\sigma}{\partial r} - \frac{\partial V_{\sigma f}}{\partial r}\frac{\partial \mathcal{I}^\sigma}{\partial \kappa} = \left(\gamma_\sigma + \frac{\partial V_{\sigma f}}{\partial r}\right)\mathcal{I}^\sigma. \tag{15}$$

Plugging the fixed and plasma-frame speeds, Eqs. (9) and (10), into equation (15) results in

$$\Rightarrow \frac{\partial \mathcal{I}^\sigma}{\partial t} + \left(v + \frac{a}{r}\right)\frac{\partial \mathcal{I}^\sigma}{\partial r} + \frac{a}{r^2}\frac{\partial \mathcal{I}^\sigma}{\partial \kappa} = \left(\gamma_\sigma - \frac{a}{r^2}\right)\mathcal{I}^\sigma, \tag{16}$$

which is desired form of the non-conservative evolution equation for the simulation.

Parameters used in the simulations are chosen as

$$\begin{aligned} r &\in [5, 50]\ R_\odot \\ a &= 10\ R_\odot^2 \mathrm{h}^{-1} \\ v &= 2.5\ R_\odot \mathrm{h}^{-1} \\ \kappa &\in [0, 10]. \end{aligned} \tag{17}$$

We consider an exponential injection spectrum for the first simulation case. The boundary conditions at the inflow boundaries of $r = 5\ R_\odot$ and $\kappa = 0$ are set as

$$\mathcal{I}^\sigma(5\ R_\odot, \kappa, t) = \mathcal{I}_0^\sigma(\kappa, t) = \mathcal{H}(t)\mathcal{H}(\kappa)e^{-q\kappa} \tag{18}$$

$$\mathcal{I}^\sigma(r, 0, t) = 0, \tag{19}$$

where $\mathcal{H}$ is the Heaviside function and q the power-spectral index of the waves, which is set to $q = 5/3$.

We derive the analytical solution of the simulation using the method of characteristics. The characteristic curves are obtained from

$$\frac{\mathrm{d}t}{1} = \frac{\mathrm{d}r}{v + a/r} = \frac{\mathrm{d}\kappa}{a/r^2} = \frac{\mathrm{d}\mathcal{I}^\sigma}{(\gamma_\sigma - a/r^2)\mathcal{I}^\sigma}.$$

The analytical solution for κ as a function of r for a wave packet that originated from (r_0, κ_0) can be found by separating and integrating,

$$\begin{aligned} \mathrm{d}\kappa &= \frac{a/r^2}{v + a/r}\mathrm{d}r \\ \Rightarrow \kappa &= \kappa_0 + \ln\frac{v + a/r_0}{v + a/r}. \end{aligned}$$

The analytical solution for the time it takes a for a wave packet that originated from (r_0, κ_0) at the time t_0 to reach (r, κ) can also be found by separating and integrating,

$$\begin{aligned} \mathrm{d}t &= \frac{r}{vr + a}\mathrm{d}r \\ \Rightarrow t &= t_0 + \frac{r - r_0}{v} - \frac{a}{v^2}\ln\frac{a + vr}{a + vr_0}. \end{aligned}$$

Using these results we can solve for the theoretical scaled intensity as a function of r, κ, and t from the second and fourth characteristic curves by integrating,

$$\begin{aligned}
\frac{\mathrm{d}r}{v + a/r} &= \frac{\mathrm{d}\mathcal{I}^\sigma}{(\gamma_\sigma - a/r^2)\mathcal{I}^\sigma} \\
\Rightarrow \frac{\mathrm{d}\mathcal{I}^\sigma}{\mathcal{I}^\sigma} &= \frac{\gamma_\sigma r^2 - a}{vr^2 + ar}\mathrm{d}r \\
\Rightarrow \ln \mathcal{I}^\sigma(r,\kappa,t) - \ln \mathcal{I}^\sigma(r_0,\kappa_0,t_0) &= \int_{r_0}^{r} \frac{\gamma_\sigma r^2 - a}{vr^2 + ar}\mathrm{d}r \\
&= \frac{\gamma_\sigma(r - r_0)}{v} + \left(1 - \frac{a\gamma_\sigma}{v^2}\right)\ln\frac{a + vr}{a + vr_0} - \ln\frac{r}{r_0} \\
&= \frac{\gamma_\sigma(r - r_0)}{v} + \ln\left(\frac{a + vr}{a + vr_0}\right)^{1 - \frac{a\gamma_\sigma}{v^2}} + \ln\frac{r_0}{r} \\
\Rightarrow \mathcal{I}^\sigma(r,\kappa,t) &= \mathcal{I}^\sigma(r_0,\kappa_0,t_0)\frac{r_0}{r}\left(\frac{a + vr}{a + vr_0}\right)^{1 - \frac{a\gamma_\sigma}{v^2}} \exp\left[\frac{\gamma_\sigma(r - r_0)}{v}\right]
\end{aligned}$$

Plugging in the boundary condition gives us

$$\mathcal{I}^\sigma(r,\kappa,t) = \mathcal{H}(t_0)\mathcal{H}(\kappa_0)e^{-q\kappa_0}\frac{r_0}{r}\left(\frac{a + vr}{a + vr_0}\right)^{1 - \frac{a\gamma_\sigma}{v^2}} \exp\left[\frac{\gamma_\sigma(r - r_0)}{v}\right],$$

which can be opened to the final form of

$$\begin{aligned}
\mathcal{I}^\sigma(r,\kappa,t) = \mathcal{H}&\left(t - \frac{r - r_0}{v} + \frac{a}{v^2}\ln\frac{a + vr}{a + vr_0}\right) \\
&\cdot \mathcal{H}\left(\kappa - \ln\frac{v + a/r_0}{v + a/r}\right) \\
&\cdot \frac{r_0}{r}\left(\frac{a + vr}{a + vr_0}\right)^{1 - \frac{a\gamma_\sigma}{v^2}}\left(\frac{v + a/r_0}{v + a/r}\right)^q \\
&\cdot \exp\left[\frac{\gamma_\sigma(r - r_0)}{v} - q\kappa\right]
\end{aligned} \tag{20}$$

for the analytical solution of the scaled intensity.

As mentioned before, the non-conservative LOD upwind implementation and the non-conserservative Lax–Wendroff scheme have been pushed to the appendix, leaving only the explicit non-conservative upwind scheme to be discussed here.

Upwind methods are schemes, where the local derivatives are solved with a linear approximation, taken as a difference of the current value and the value of an upwind simulation cell. Upwind schemes are a very common way to handle wave

evolution equations, because of their simplicity, though linear approximation of the local derivatives can cause high amounts of diffusion with insufficient resolutions and without implementations, such as *anti-diffusion operators*.

Our first iteration of an upwind scheme is explicit in time, meaning that the value of the time derivative between t_n and t_{n+1} is evaluated using information at the previous time step, t_n, only. (An implicit implementation would use information on the next time step, t_{n+1}, as well.) The calculations do not apply to the injection cells of the system, which are instead pre-scribed. The non-conservative advection equation (15) can be derived to the following form that is fit for simulation:

$$\mathcal{I}^{\sigma}_{r,\kappa,t+\Delta t} = \left[\mathcal{I}^{\sigma}_{r,\kappa,t} - \Delta t\left(v + \frac{a}{r}\right)\frac{\partial \mathcal{I}^{\sigma}_{r,\kappa,t}}{\partial r} - \Delta t\frac{a}{r^2}\frac{\partial \mathcal{I}^{\sigma}_{r,k,t}}{\partial \kappa}\right]\exp\left(\Delta t\left(\gamma_\sigma - \frac{a}{r^2}\right)\right), \quad (21)$$

where the derivatives are defined as

$$\frac{\partial \mathcal{I}^{\sigma}_{r_i,\kappa,t}}{\partial r} = \begin{cases} \dfrac{\mathcal{I}^{\sigma}_{r_i,\kappa,t} - \mathcal{I}^{\sigma}_{r_{i-1},\kappa,t}}{r_i - r_{i-1}}, & \dot{r}(r,\kappa,t) \geq 0 \\ \dfrac{\mathcal{I}^{\sigma}_{r_{i+1},\kappa,t} - \mathcal{I}^{\sigma}_{r_i,\kappa,t}}{r_{i+1} - r_i}, & \dot{r}(r,\kappa,t) < 0 \end{cases} \quad (22)$$

$$\frac{\partial \mathcal{I}^{\sigma}_{r,\kappa_i,t}}{\partial \kappa} = \begin{cases} \dfrac{\mathcal{I}^{\sigma}_{r,\kappa_i,t} - \mathcal{I}^{\sigma}_{r,\kappa_{i-1},t}}{\kappa_i - \kappa_{i-1}}, & \dot{\kappa}(r,\kappa,t) \geq 0 \\ \dfrac{\mathcal{I}^{\sigma}_{r,\kappa_{i+1},t} - \mathcal{I}^{\sigma}_{r,\kappa_i,t}}{\kappa_{i+1} - \kappa_i}, & \dot{\kappa}(r,\kappa,t) < 0 \end{cases} \quad (23)$$

The upwind schemes need to fulfill the *Courant–Friedrichs–Lewy* (CFL) condition. The condition requires for a one-dimensional case for the time step to be smaller than the time taken for the wave packet to propagate the distance Δx,

$$\frac{c\Delta t}{\Delta x} \leq 1, \quad (24)$$

where c is the the (positive) velocity of the wave packet, Δx the size of the simulation cell, and Δt the size of the time step. [27]

For our simulation and the two-dimensional case the CFL-condition reads as

$$\frac{1}{\Delta t} = \frac{\dot{r}}{\Delta r} + \frac{\dot{\kappa}}{\Delta \kappa}, \quad (25)$$

where Δr and $\Delta\kappa$ are grid parameters chosen to satisfy accuracy and computation time. Δt will be calculated in each simulation cell on the grid and the smallest Δt is chosen so that the clause is satisfied at each cell on the grid.

2.2.2 Conservative Flux Equations

Conservative flux equations paired with conservative numerical schemes are a physically more accurate way to describe the evolution of the fluxes, due to the conservation of the flux terms. Finite difference methods, such as the upwind scheme, are not necessarily conservative in all cases but can in simple advection cases correspond to the Godunov method, which is a conservative finite volume method [28, 29]. Our simulation case is not simple enough to regard the upwind scheme as a conservative numerical scheme, but instead explores the suitability of the upwind method in the case of variable velocity and conservative equations.

Starting again from equation (13) we can derive a conservative form for the magnetic intensity advection equation. This time we'll denote a different scaled magnetic intensity as follows:

$$\mathfrak{I}^\sigma = \frac{V_{\sigma f}}{V_\sigma} r^2 k I^\sigma. \tag{26}$$

Multiplying equation (13) by r^2k results in

$$\Rightarrow \frac{\partial}{\partial t}\left(r^2 k \frac{V_{\sigma f}}{V_\sigma} I^\sigma\right) + \frac{\partial}{\partial r}\left(r^2 k \frac{V_{\sigma f}^2}{V_\sigma} I^\sigma\right) - k\frac{\partial}{\partial k}\left(k\frac{\partial V_{\sigma f}}{\partial r} r^2 \frac{V_{\sigma f}}{V_\sigma} I^\sigma\right) = \gamma_\sigma r^2 k \frac{V_{\sigma f}}{V_\sigma} I^\sigma.$$

Changing to the scaled magnetic intensity $\mathfrak{I}^\sigma$ results in

$$\Rightarrow \frac{\partial}{\partial t}(\mathfrak{I}^\sigma) + \frac{\partial}{\partial r}(V_{\sigma f}\mathfrak{I}^\sigma) - k\frac{\partial}{\partial k}\left(\frac{\partial V_{\sigma f}}{\partial r}\mathfrak{I}^\sigma\right) = \gamma_\sigma \mathfrak{I}^\sigma.$$

Plugging in the logarithmic term $\kappa = \ln\frac{k}{k_0}$ results in

$$\Rightarrow \frac{\partial}{\partial t}(\mathfrak{I}^\sigma) + \frac{\partial}{\partial r}(V_{\sigma f}\mathfrak{I}^\sigma) + \frac{\partial}{\partial \kappa}\left(-\frac{\partial V_{\sigma f}}{\partial r}\mathfrak{I}^\sigma\right) = \gamma_\sigma \mathfrak{I}^\sigma. \tag{27}$$

the fixed and plasma-frame speeds are again defined as in equations (7), (8), (9), and (10). Plugging these into equation (27) results in

$$\Rightarrow \frac{\partial \mathfrak{I}^\sigma}{\partial t} + \frac{\partial}{\partial r}\underbrace{\left[\left(v + \frac{a}{r}\right)\mathfrak{I}^\sigma\right]}_{F_r} + \frac{\partial}{\partial \kappa}\underbrace{\left[\frac{a}{r^2}\mathfrak{I}^\sigma\right]}_{F_\kappa} = \gamma_\sigma \mathfrak{I}^\sigma, \tag{28}$$

where the wave intensity fluxes in r- and κ-direction are denoted as F_r and F_κ. This is the desired form of the conservative evolution equation used for the simulation.

Parameters used in the simulations are the same as before, which are denoted in equations (17). The boundary conditions at the inflow boundaries of $r = 5\ R_\odot$ and $\kappa = 0$ are again set as

$$\mathfrak{I}^\sigma(5\ R_\odot, \kappa, t) = \mathfrak{I}_0^\sigma(\kappa, t) = \mathcal{H}(t)\mathcal{H}(\kappa)e^{-q\kappa} \tag{18}$$

$$\mathfrak{I}^\sigma(r, 0, t) = 0, \tag{19}$$

where q is now set to a value of unity lower, $q = 2/3$, due to the scaled magnetic intensity's definition containing and additional k-term.

We derive the analytical solution of the simulation using the method of characteristics. The characteristic curves are obtained from

$$\frac{\mathrm{d}t}{1} = \frac{\mathrm{d}r}{v + a/r} = \frac{\mathrm{d}\kappa}{a/r^2} = \frac{\mathrm{d}\mathfrak{I}^\sigma}{(\gamma_\sigma + a/r^2)\mathfrak{I}^\sigma}.$$

The analytical solution for κ as a function of r for a wave packet that originated from (r_0, κ_0) can be found by separating and integrating,

$$\mathrm{d}\kappa = \frac{a/r^2}{v + a/r}\mathrm{d}r$$
$$\Rightarrow \kappa = \kappa_0 + \ln\frac{v + a/r_0}{v + a/r}.$$

The analytical solution for the time it takes a for a wave packet that originated from (r_0, κ_0) at the time t_0 to reach (r, κ) can also be found by separating and integrating,

$$\mathrm{d}t = \frac{r}{vr + a}\mathrm{d}r$$
$$\Rightarrow t = t_0 + \frac{r - r_0}{v} - \frac{a}{v^2}\ln\frac{a + vr}{a + vr_0}.$$

Using these results we can solve for the theoretical scaled intensity as a function of r, κ, and t from the second and fourth characteristic curves by integrating,

$$\begin{aligned}
\frac{\mathrm{d}r}{v+a/r} &= \frac{\mathrm{d}\mathfrak{I}^\sigma}{(\gamma_\sigma + a/r^2)\mathfrak{I}^\sigma} \\
\Rightarrow \frac{\mathrm{d}\mathfrak{I}^\sigma}{\mathfrak{I}^\sigma} &= \frac{\gamma_\sigma r^2 + a}{vr^2 + ar}\mathrm{d}r \\
\Rightarrow \ln\,\mathfrak{I}^\sigma(r,\kappa,t) - \ln\,\mathfrak{I}^\sigma(r_0,\kappa_0,t_0) &= \int_{r_0}^{r} \frac{\gamma_\sigma r^2 + a}{vr^2 + ar}\mathrm{d}r \\
&= \frac{\gamma_\sigma(r-r_0)}{v} - \left(1 + \frac{a\gamma_\sigma}{v^2}\right)\ln\,\frac{a+vr}{a+vr_0} - \ln\,\frac{r}{r_0} \\
&= \frac{\gamma_\sigma(r-r_0)}{v} + \ln\,\left(\frac{a+vr}{a+vr_0}\right)^{-1-\frac{a\gamma_\sigma}{v^2}} + \ln\,\frac{r_0}{r} \\
\Rightarrow \mathfrak{I}^\sigma(r,\kappa,t) &= \mathfrak{I}^\sigma(r_0,\kappa_0,t_0)\frac{r_0}{r}\left(\frac{a+vr}{a+vr_0}\right)^{-1-\frac{a\gamma_\sigma}{v^2}} \exp\left[\frac{\gamma_\sigma(r-r_0)}{v}\right]
\end{aligned}$$

Plugging in the boundary condition gives us

$$\mathfrak{I}^\sigma(r,\kappa,t) = \mathcal{H}(t_0)\mathcal{H}(\kappa_0)e^{-q\kappa_0}\frac{r_0}{r}\left(\frac{a+vr}{a+vr_0}\right)^{-1-\frac{a\gamma_\sigma}{v^2}} \exp\left[\frac{\gamma_\sigma(r-r_0)}{v}\right],$$

which can be opened to the final form of

$$\begin{aligned}
\mathfrak{I}^\sigma(r,\kappa,t) = \mathcal{H}&\left(t - \frac{r-r_0}{v} + \frac{a}{v^2}\ln\frac{a+vr}{a+vr_0}\right) \\
&\cdot \mathcal{H}\left(\kappa - \ln\frac{v+a/r_0}{v+a/r}\right) \\
&\cdot \frac{r_0}{r}\left(\frac{a+vr}{a+vr_0}\right)^{-1-\frac{a\gamma_\sigma}{v^2}}\left(\frac{v+a/r_0}{v+a/r}\right)^{q} \\
&\cdot \exp\left[\frac{\gamma_\sigma(r-r_0)}{v} - q\kappa\right]
\end{aligned} \tag{29}$$

for the analytical solution of the scaled intensity.

2.2.2.1 Conservative Upwind Scheme For the conservative upwind scheme equation (28) is derived to a similar explicit form of equation (21) presented in section 2.2.2.1:

$$\begin{aligned}
\mathfrak{I}^\sigma_{r,\kappa,t+\Delta t} = &\left[\mathfrak{I}^\sigma_{r,\kappa,t} - \Delta t\frac{\partial}{\partial r}\underbrace{\left(\left(v + \frac{a}{r}\right)\mathfrak{I}^\sigma_{r,\kappa,t}\right)}_{F_r} - \Delta t\frac{\partial}{\partial \kappa}\underbrace{\left(\frac{a}{r^2}\mathfrak{I}^\sigma_{r,k,t}\right)}_{F_\kappa}\right] \\
&\cdot \exp\left(\Delta t\left(\gamma_\sigma + \frac{a}{(r-(v+a/r)\Delta t/2)^2}\right)\right),
\end{aligned} \tag{30}$$

where the derivatives are defined as

$$\frac{\partial F_{r_i}}{\partial r} = \begin{cases} \dfrac{(v+\frac{a}{r_i})\mathfrak{I}^{\sigma}_{r_i,\kappa,t+\frac{1}{3}\Delta t} - (v+\frac{a}{r_{i-1}})\mathfrak{I}^{\sigma}_{r_{i-1},\kappa,t}}{r_i - r_{i-1}}, & \dot{r}(r,\kappa,t) \geq 0 \\ \dfrac{(v+\frac{a}{r_{i+1}})\mathfrak{I}^{\sigma}_{r_{i+1},\kappa,t+\frac{1}{3}\Delta t} - (v+\frac{a}{r_i})\mathfrak{I}^{\sigma}_{r_i,\kappa,t}}{r_{i+1} - r_i}, & \dot{r}(r,\kappa,t) < 0 \end{cases} \tag{31}$$

$$\frac{\partial F_{\kappa_i}}{\partial \kappa} = \begin{cases} \dfrac{\frac{a}{r^2}(\mathfrak{I}^{\sigma}_{r,\kappa_i,t+\frac{2}{3}\Delta t} - \mathfrak{I}^{\sigma}_{r,\kappa_{i-1},t})}{\kappa_i - \kappa_{i-1}}, & \dot{\kappa}(r,\kappa,t) \geq 0 \\ \dfrac{\frac{a}{r^2}(\mathfrak{I}^{\sigma}_{r,\kappa_{i+1},t+\frac{2}{3}\Delta t} - \mathfrak{I}^{\sigma}_{r,\kappa_i,t})}{\kappa_{i+1} - \kappa_i}, & \dot{\kappa}(r,\kappa,t) < 0, \end{cases} \tag{32}$$

and the growth term is evaluated at the wave front's location at halfway of the time step.

Again, the same stability conditions apply as in the non-conservative upwind scheme (equations (24) and (25)) [27].

2.2.2.2 Conservative Lax-Wendroff Scheme The Lax-Wendroff scheme uses the same evolution equation (30) as the conservative upwind scheme, but the growth is instead calculated at the wave front's location at the start of the time step:

$$\begin{aligned} \mathfrak{I}^{\sigma}_{r,\kappa,t+\Delta t} = \Bigg[\mathfrak{I}^{\sigma}_{r,\kappa,t} - \Delta t \frac{\partial}{\partial r} \underbrace{\left(\left(v + \frac{a}{r} \right) \mathfrak{I}^{\sigma}_{r,\kappa,t} \right)}_{F_r} - \Delta t \frac{\partial}{\partial \kappa} \underbrace{\left(\frac{a}{r^2} \mathfrak{I}^{\sigma}_{r,k,t} \right)}_{F_\kappa} \Bigg] \\ \cdot \exp\left(\Delta t \left(\gamma_\sigma + \frac{a}{r^2} \right) \right), \end{aligned} \tag{33}$$

where the derivatives are defined as

$$\begin{aligned}
\frac{\partial F_{r_i}}{\partial r} &= \frac{1}{\Delta r}(\mathfrak{I}^{\sigma}_{r_{i+\frac{1}{2}},\kappa,t+\frac{1}{2}\Delta t} - \mathfrak{I}^{\sigma}_{r_{i-\frac{1}{2}},\kappa,t+\frac{1}{2}\Delta t}) \\
\mathfrak{I}^{\sigma}_{r_{i+\frac{1}{2}},\kappa,t+\frac{1}{2}\Delta t} &= \frac{1}{2}(\mathfrak{I}^{\sigma}_{r_{i+1},\kappa,t} + \mathfrak{I}^{\sigma}_{r_i,\kappa,t}) \\
&\quad - \frac{\Delta t}{2\Delta r}\left(\left(v + \frac{a}{r_{i+1}}\right)\mathfrak{I}^{\sigma}_{r_{i+1},\kappa,t} - \left(v + \frac{a}{r_i}\right)\mathfrak{I}^{\sigma}_{r_i,\kappa,t}\right) \qquad (34) \\
\mathfrak{I}^{\sigma}_{r_{i-\frac{1}{2}},\kappa,t+\frac{1}{2}\Delta t} &= \frac{1}{2}(\mathfrak{I}^{\sigma}_{r_i,\kappa,t} + \mathfrak{I}^{\sigma}_{r_{i-1},\kappa,t}) \\
&\quad - \frac{\Delta t}{2\Delta r}\left(\left(v + \frac{a}{r_i}\right)\mathfrak{I}^{\sigma}_{r_i,\kappa,t} - \left(v + \frac{a}{r_{i-1}}\right)\mathfrak{I}^{\sigma}_{r_{i-1},\kappa,t}\right) \\
\frac{\partial F_{\kappa_i}}{\partial \kappa} &= \frac{1}{\Delta \kappa}(\mathfrak{I}^{\sigma}_{r,\kappa_{i+\frac{1}{2}},t+\frac{1}{2}\Delta t} - \mathfrak{I}^{\sigma}_{r,\kappa_{i-\frac{1}{2}},t+\frac{1}{2}\Delta t}) \\
\mathfrak{I}^{\sigma}_{r,\kappa_{i+\frac{1}{2}},t+\frac{1}{2}\Delta t} &= \frac{1}{2}(\mathfrak{I}^{\sigma}_{r,\kappa_{i+1},t} + \mathfrak{I}^{\sigma}_{r,\kappa_i,t}) - \frac{\Delta t}{2\Delta \kappa}\left(\frac{a}{r^2}\right)(\mathfrak{I}^{\sigma}_{r,\kappa_{i+1},t} - \mathfrak{I}^{\sigma}_{r,\kappa_i,t}) \qquad (35) \\
\mathfrak{I}^{\sigma}_{r,\kappa_{i-\frac{1}{2}},t+\frac{1}{2}\Delta t} &= \frac{1}{2}(\mathfrak{I}^{\sigma}_{r,\kappa_i,t} + \mathfrak{I}^{\sigma}_{r,\kappa_{i-1},t}) - \frac{\Delta t}{2\Delta \kappa}\left(\frac{a}{r^2}\right)(\mathfrak{I}^{\sigma}_{r,\kappa_i,t} - \mathfrak{I}^{\sigma}_{r,\kappa_{i-1},t})
\end{aligned}$$

Again, the same stability conditions apply as in the non-conservative Lax–Wendroff scheme (equations (24) and (25)) [27].

2.2.3 Semi-Lagrangian Scheme

As an effort to remove diffusion entirely, semi-Lagrangian methods are considered. Instead of observing spatial cells, as one does in an Eulerian method, Lagrangian methods observe the wave packets themselves. In a semi-Lagrangian scheme the base of the simulation is Eulerian, but the governing equations are Lagrangian. In our case, a specialized grid is constructed for the wave propagation. The r-grid is defined so that the size of the cell is exactly the distance a wave packet would travel in a single time step. This removes the need to calculate derivatives for the propagation, removing also the diffusion problem entirely. This model simulates wave evolution accurately, but has its own nuisances. The derivation of the grid defining equations is case specific, which can be cumbersome.

Starting again from equation (13) we can derive a form for the scaled magnetic

intensity evolution equation. This time we'll denote the scaled spectral magnetic intensity as follows:

$$\mathbb{I}^\sigma = \frac{V_{\sigma f}^2}{V_\sigma} r^2 k I^\sigma. \tag{36}$$

Multiplying equation (13) by $V_{\sigma f} r^2 k$ results in

$$\frac{\partial}{\partial t}\left(r^2 k \frac{V_{\sigma f}^2}{V_\sigma} I^\sigma\right) + V_{\sigma f}\frac{\partial}{\partial r}\left(r^2 k \frac{V_{\sigma f}^3}{V_\sigma} I^\sigma\right) - k\frac{\partial}{\partial k}\left(k\frac{\partial V_{\sigma f}}{\partial r} r^2 \frac{V_{\sigma f}^2}{V_\sigma} I^\sigma\right) = \gamma_\sigma r^2 k \frac{V_{\sigma f}^2}{V_\sigma} I^\sigma.$$

Changing to the scaled magnetic intensity $\mathbb{I}^\sigma$ results in

$$\Rightarrow \frac{\partial}{\partial t}(\mathbb{I}^\sigma) + V_{\sigma f}\frac{\partial}{\partial r}(\mathbb{I}^\sigma) - k\frac{\partial V_{\sigma f}}{\partial r}\frac{\partial}{\partial k}(\mathbb{I}^\sigma) = \gamma_\sigma \mathbb{I}^\sigma. \tag{37}$$

Next we change from k-space to ω-space. The decision of using ω instead of k becomes apparent when we write

$$\omega = V_{\sigma f} k,$$

where ω is the angular wave frequency, and observe one of the characteristic equations from equation (37):

$$-\left(\frac{\partial V_{\sigma_f}}{\partial r}\right)^{-1}\frac{\mathrm{d}k}{k} = \frac{\mathrm{d}r}{V_{\sigma f}}$$
$$\Rightarrow \frac{\mathrm{d}k}{k} = -\frac{1}{V_{\sigma f}}\frac{\partial V_{\sigma_f}}{\partial r}\mathrm{d}r = -\frac{\mathrm{d}V_{\sigma f}}{V_{\sigma f}},$$

and comparing this to

$$\mathrm{d}\omega = \mathrm{d}(V_{\sigma f}k) = \mathrm{d}V_{\sigma f}k + \mathrm{d}k V_{\sigma f} = V_{\sigma f}k\left(\frac{\mathrm{d}k}{k} + \frac{\mathrm{d}V_{\sigma f}}{V_{\sigma f}}\right) = 0$$

we see that ω is constant along characteristic lines, meaning that no wave transport occurs in the ω-direction. Considering the partial derivatives after the coordinate transform from (r, k) to (r, ω)

$$\frac{\partial}{\partial t} \to \frac{\partial}{\partial t}$$
$$\frac{\partial}{\partial r} \to \frac{\partial}{\partial r} + \frac{\partial \omega}{\partial r}\frac{\partial}{\partial \omega} = \frac{\partial}{\partial r} + k\frac{\partial V_{\sigma f}}{\partial r}\frac{\partial}{\partial \omega}$$
$$\frac{\partial}{\partial k} \to \frac{\partial \omega}{\partial k}\frac{\partial}{\partial \omega} = V_{\sigma f}\frac{\partial}{\partial \omega}$$

and using ω as the second coordinate in equation (37), we can write

$$\frac{\partial \mathbb{I}^{\sigma}_{\omega}}{\partial t} + V_{\sigma f}\frac{\partial \mathbb{I}^{\sigma}_{\omega}}{\partial r} + V_{\sigma f}k\frac{\partial V_{\sigma f}}{\partial r}\frac{\partial \mathbb{I}^{\sigma}_{\omega}}{\partial \omega} - k\frac{\partial V_{\sigma f}}{\partial r}V_{\sigma f}\frac{\partial \mathbb{I}^{\sigma}_{\omega}}{\partial \omega} = \gamma_{\sigma}\mathbb{I}^{\sigma}_{\omega},$$

which simplifies to

$$\frac{\partial \mathbb{I}^{\sigma}_{\omega}}{\partial t} + V_{\sigma f}\frac{\partial \mathbb{I}^{\sigma}_{\omega}}{\partial r} = \gamma_{\sigma}\mathbb{I}^{\sigma}_{\omega}. \tag{38}$$

In semi-Lagrangian formalism, we can propagate the solution from a grid point to the next by defining the distances between spatial points as the exact length a wave packet travels in a time step,

$$\Delta t = \int_{r_i}^{r_{i+1}} \frac{\mathrm{d}r}{V_{\sigma f}}. \tag{39}$$

The distance from r_0 to r_1 is manually chosen as a parameter, the time step then computed, and the rest of the grid is then calculated from this value.

The fixed frame and plasma-frame speeds, $V_{\sigma f}$ and V_{σ}, are again chosen to be the same as in equations (7), (8), (9), and (10).

Taking

$$a = 10\ R_{\odot}^{2}\mathrm{h}^{-1}$$
$$v = 2.5\ R_{\odot}\mathrm{h}^{-1},$$

we can now solve the r-grid levels from equation (39):

$$\Delta t = \int_{r_i}^{r_{i+1}} \frac{\mathrm{d}r}{v + a/r} = \frac{r_{i+1} - r_i}{v} + \frac{a}{v^2}\ln\frac{a + vr_i}{a + vr_{i+1}}.$$

Denoting $r_{i+1} = r_i + \Delta r_i$ results in

$$\Delta t = \frac{\Delta r_i}{v} - \frac{a}{v^2}\ln\left(1 + \frac{v\Delta r_i}{a + vr_i}\right),$$

which can be solved iteratively as

$$\Delta r_i^{(n+1)} = v\Delta t + \frac{a}{v}\ln\left(1 + \frac{v\Delta r_i^{(n)}}{a + vr_i}\right), \tag{40}$$

where we use the initial choice of r_0 and r_1 as

$$\Delta r_i^{(0)} = \Delta r_{i-1}.$$

Choosing $r_0 = 5\ R_\odot$ and $r_1 = r_0 + \Delta r_0 = r_0 + R_\odot$ should make Δr_i converge to a good value since $\Delta r_i < r_i$ is fulfilled. Smaller values for Δr_0 can be chosen increasing the computation cost of the simulation.

The analytical solution can be obtained again from the characteristic curves of equation (38):

$$\frac{\mathrm{d}t}{1} = \frac{\mathrm{d}r}{v + a/r} = \frac{\mathrm{d}\mathbb{I}_\omega^\sigma}{\gamma_\sigma \mathbb{I}_\omega^\sigma}.$$

Solving for the analytical time from the first and second characteristic curves:

$$\begin{aligned} \mathrm{d}t &= \frac{r}{vr + a}\mathrm{d}r \\ \Rightarrow t &= t_0 + \frac{r - r_0}{v} - \frac{a}{v^2}\ln\frac{a + vr}{a + vr_0}. \end{aligned}$$

The scaled spectral magnetic intensity is then solved from the first and last characteristic curves:

$$\begin{aligned} \frac{\mathrm{d}\mathbb{I}_\omega^\sigma}{\gamma_\sigma \mathbb{I}_\omega^\sigma} &= \mathrm{d}t \\ \Rightarrow \ln\frac{\mathbb{I}_\omega^\sigma(r,t)}{\mathbb{I}_\omega^\sigma(r_0,t_0)} &= \gamma_\sigma(t - t_0) \\ &= \gamma_\sigma\left(\frac{r - r_0}{v} - \frac{a}{v^2}\ln\frac{a + vr}{a + vr_0}\right) \\ \Rightarrow \mathbb{I}_\omega^\sigma(r,t) &= \mathbb{I}_{\omega,0}^\sigma(t_0)\exp\left[\gamma_\sigma\left(\frac{r - r_0}{v} - \frac{a}{v^2}\ln\frac{a + vr}{a + vr_0}\right)\right], \end{aligned} \tag{41}$$

where $\mathbb{I}_{\omega,0}^\sigma(t_0)$ is the boundary condition set for the system.

As the equations have no dependency on the wave angular frequency, ω, we choose to use a logarithmic variable $w = \ln\frac{\omega}{\omega_0}$ to reduce the computational load

and to cover a wide range of angular frequencies. The boundaries of the simulation box are chosen as

$$r \in [5, 50]\ R_\odot$$

$$w \in [0, 10]$$

to have enough coverage of the system. The boundary condition is defined similar to the earlier cases, now only in w-space:

$$\mathbb{I}^\sigma_\omega(5\ R_\odot, w, t) = \mathcal{H}(t)e^{-qw}, \tag{42}$$

where $q = 2/3$ due to the definition of the scaled spectral magnetic intensity.

Next we derive the evolution equation (38) to a form used in the simulations, where the wave growth rate of the waves is implemented as a semi-implicit operator,

$$\mathbb{I}^\sigma_\omega(r_i, w, t + \Delta t) = \mathbb{I}^\sigma_\omega(r_{i-1}, w, t)\frac{1 + \frac{1}{2}\gamma_\sigma \Delta t}{1 - \frac{1}{2}\gamma_\sigma \Delta t}. \tag{43}$$

As is clear, the implemented equations are very simple, with no derivative calculations as the grid definition already takes care of the correct propagation of the waves.

2.2.4 Resolution Refiner

In addition to the semi-Lagrangian simulation implementation, a tool to dynamically increase and decrease the simulation's resolution was developed. As the waves propagate "cleanly" through the simulation, a time size can be determined for each cell describing how long the intensity spends in a cell. As a cell is split or merged the physical size and the temporal size of the cell are altered, so in physically smaller cells the wave moves to the next cell faster. The tool was developed so that each simulation grid r-column can be split into two as many times as needed by any kind of boolean clause, making the model quite flexible regarding conditions for resolution changes.

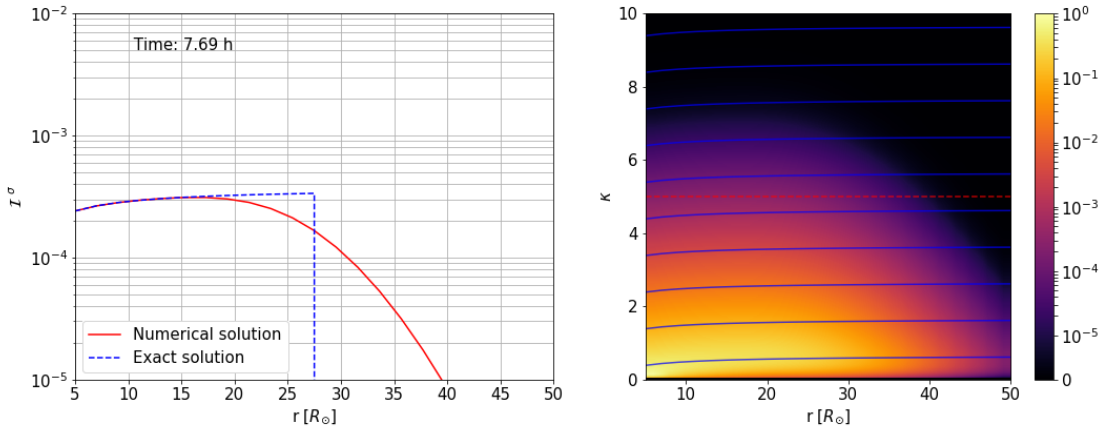

Figure 2. A non-conservative upwind simulation at the state where the analytical solution has reached approximately the halfway of the simulation box. The plot on the left contains a slice parallel to the r-axis denoted by the red dashed line in the plot on the right. The streamlines of the analytical solution are plotted as the blue lines on the plot on the right. The scaled intensity $\mathcal{I}^\sigma$ is denoted as a color gradient on the plot on the right. The simulation parameters used are $\Delta r = 2\ R_\odot$, $\Delta\kappa = 0.1$, and $\gamma = 0$.

2.3 Results

The figures of the simulation will contain the two-dimensional wave space with color indicating intensity (right) and a slice of the data in r-direction to analyze the profile and compare it to the theoretical solutions (left). The plots on the right will also have the analytical streamlines plotted for comparing the propagation of the wave front to the analytical case.

2.3.1 Non-conservative Upwind Scheme

A non-conservative upwind simulation can be seen in figures 2 and 3, where Fig. 2 shows the point where the wave front has propagated half of the simulation box and Fig. 3 shows the end of the simulation where the wave spectrum is stable.

Looking at Fig. 2 one can immediately detect a large amount of diffusion, which is an effect of the resolution and derivative calculation. Upwind schemes would require very fine resolutions to increase accuracy at the cost of computation time

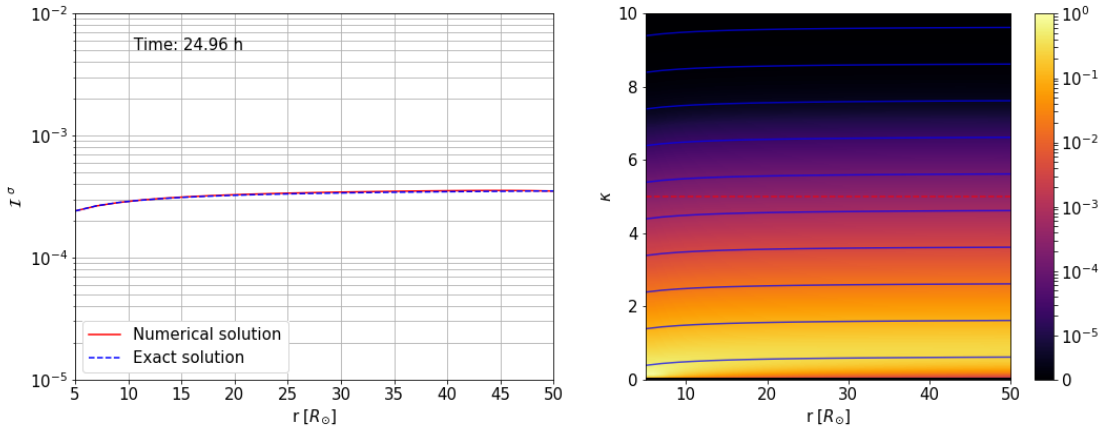

Figure 3. The steady state of the non-conservative upwind simulation presented in figure 2. The plot on the left contains a slice parallel to the r-axis denoted by the red dashed line in the plot on the right. The streamlines of the analytical solution are plotted as the blue lines on the plot on the right. The scaled intensity $\mathcal{I}^\sigma$ is denoted as a color gradient on the plot on the right. The simulation parameters used are $\Delta r = 2\ R_\odot$, $\Delta\kappa = 0.1$, and $\gamma = 0$.

or implementations of *anti-diffusion operators*. These operators were deemed useful and possible numerical implementations to explore, albeit their tendency to increase the computational load, but were ultimately out of the scope of this thesis. More on combating diffusion through numerical means and models can be read in e.g. [30–33].

As a steady state solver the upwind scheme works fine, as we can see in figure 3. The final values of the scaled intensity correspond with the analytical solution and as such can be used for steady state solutions.

2.3.2 Conservative Upwind Scheme

The results of the conservative upwind scheme can seen in figures 4–7 for the cases of $\gamma_\sigma = 0$ and $\gamma_\sigma = 1$. For the $\gamma_\sigma = 0$ simulation, where the resolution is coarser, the diffusion is still about the same magnitude as in the non-conservative upwind scheme (figure 2), but now a small deviation from the analytical value can be detected. Increasing the resolution, as was done in the $\gamma_\sigma = 1$ case, significantly

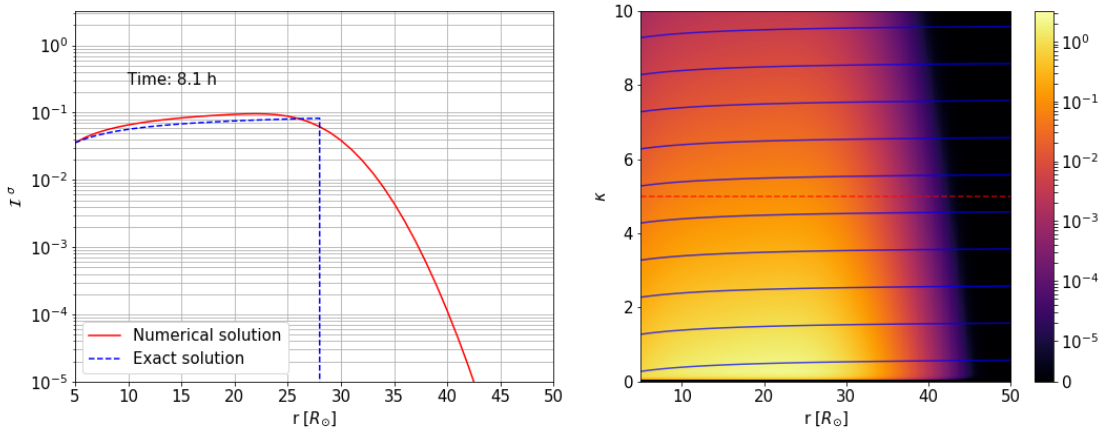

Figure 4. A conservative upwind simulation at the state where the analytical solution has reached approximately the halfway of the simulation box. The plot on the left contains a slice parallel to the r-axis denoted by the red dashed line in the plot on the right. The streamlines of the analytical solution are plotted as the blue lines on the plot on the right. The scaled intensity $\mathcal{I}^\sigma$ is denoted as a color gradient on the plot on the right. The simulation parameters used are $\Delta r = 1\ R_\odot$, $\Delta\kappa = 0.1$, and $\gamma = 0$

reduces the diffusion. Comparing figures 5 and 7 we can see that the discrepancy grows in areas with more intense intensity growth, but is also reduced by finer resolution. The conservative upwind scheme works as a steady state solver, but is computationally much heavier than its non-conservative counterpart. The conservative upwind scheme alone then doesn't bring anything more to the table compared to the non-conservative upwind scheme.

2.3.3 Conservative Lax–Wendroff Scheme

The results of the conservative Lax–Wendroff simulations can be seen in figures 8–11 for the cases of $\gamma_\sigma = 0$ and $\gamma_\sigma = 1$. The conservative Lax–Wendroff scheme offers a bit smaller diffusion and a match to the analytical solutions in the steady state in both cases of γ_σ. The oscillation mentioned in the non-conservative Lax–Wendroff scheme is still present but, as discussed before, it can be reduced with a finer resolution. Refining the resolution also lessens the diffusion as can be seen when comparing figures 8 and 10. As a side effect the Lax–Wendroff has stability

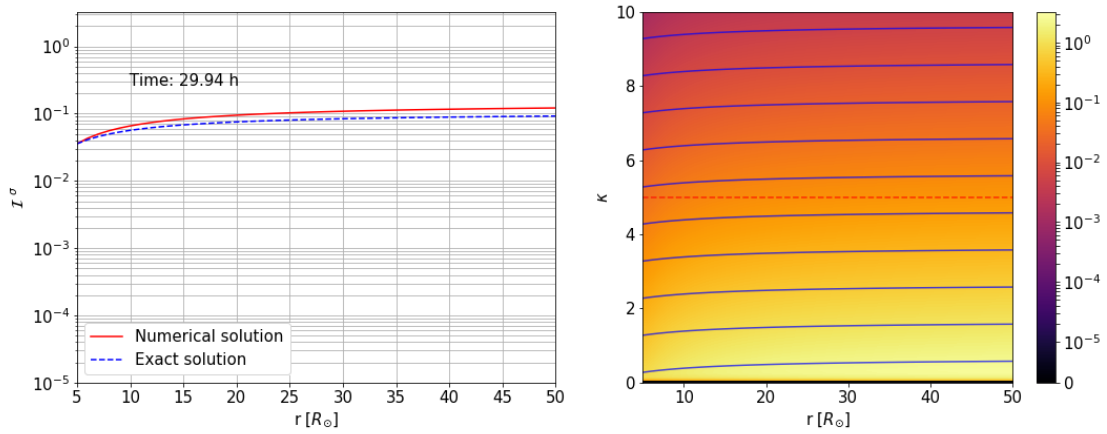

Figure 5. The steady state of the conservative upwind simulation presented in figure 4. The plot on the left contains a slice parallel to the r-axis denoted by the red dashed line in the plot on the right. The streamlines of the analytical solution are plotted as the blue lines on the plot on the right. The scaled intensity $\mathcal{I}^\sigma$ is denoted as a color gradient on the plot on the right. The simulation parameters used are $\Delta r = 1\ R_\odot$, $\Delta\kappa = 0.1$, and $\gamma = 0$

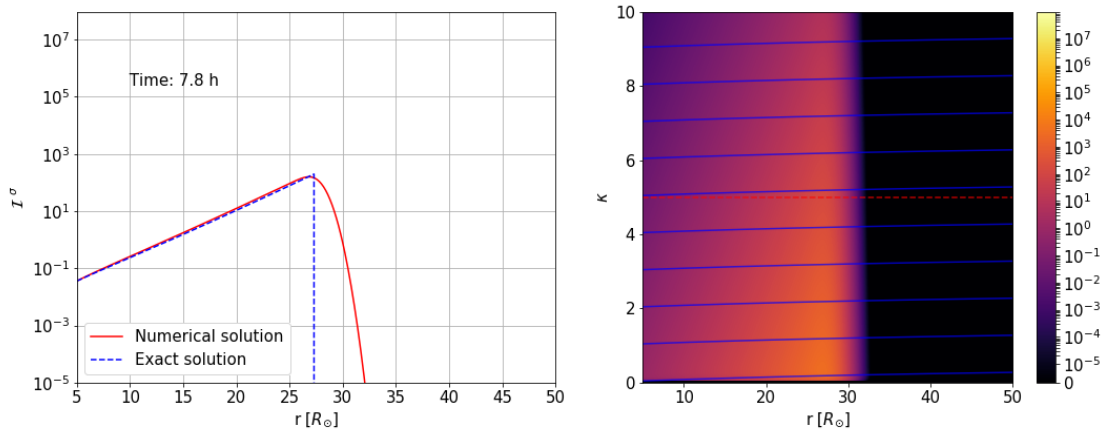

Figure 6. A conservative upwind simulation at the state where the analytical solution has reached approximately the halfway of the simulation box. The plot on the left contains a slice parallel to the r-axis denoted by the red dashed line in the plot on the right. The streamlines of the analytical solution are plotted as the blue lines on the plot on the right. The scaled intensity $\mathcal{I}^\sigma$ is denoted as a color gradient on the plot on the right. The simulation parameters used are $\Delta r = 0.1\ R_\odot$, $\Delta\kappa = 0.1$, and $\gamma = 1$

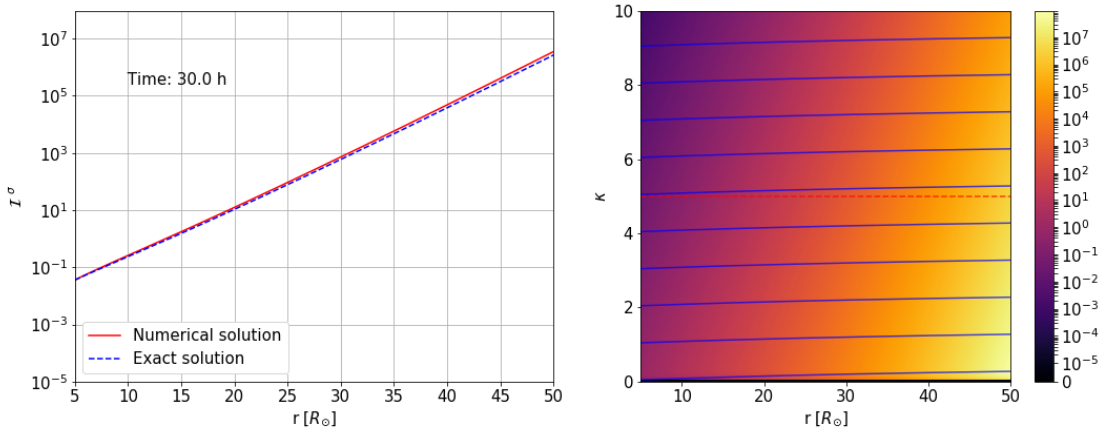

Figure 7. The steady state of the conservative upwind simulation presented in figure 6. The plot on the left contains a slice parallel to the r-axis denoted by the red dashed line in the plot on the right. The streamlines of the analytical solution are plotted as the blue lines on the plot on the right. The scaled intensity $\mathcal{I}^\sigma$ is denoted as a color gradient on the plot on the right. The simulation parameters used are $\Delta r = 0.1\ R_\odot$, $\Delta\kappa = 0.1$, and $\gamma = 1$

issues at the low wave number boundary, causing negative values to arise due to the oscillating nature of the solution. Investigation of the boundary effects should be commenced to see if they could be removed, but were not done for this model.

2.3.4 Semi-Lagrangian Scheme

The results for the semi-Lagrangian scheme with $\gamma_\sigma = 0$ and $\gamma_\sigma = 1$ can be seen in figures 12–15. As we can see in figures 12 and 14 no diffusion is present in either case and the simulation matches the analytical solution very well. This is to be expected from a semi-Lagrangian scheme as the grid itself takes care of the propagation of the waves. Looking at the steady states 13 and 15 we can see that the simulation is perfectly good also for steady state solving and is not too dependent on a fine resolution of the r-axis as the simulation times were relatively low. The simulation grid can be solved from non-analytical settings, making the scheme in this regard good for wave transport solving, since it is not then limited by the setting of the problem, though one must be careful with accuracy and stability if solving non-

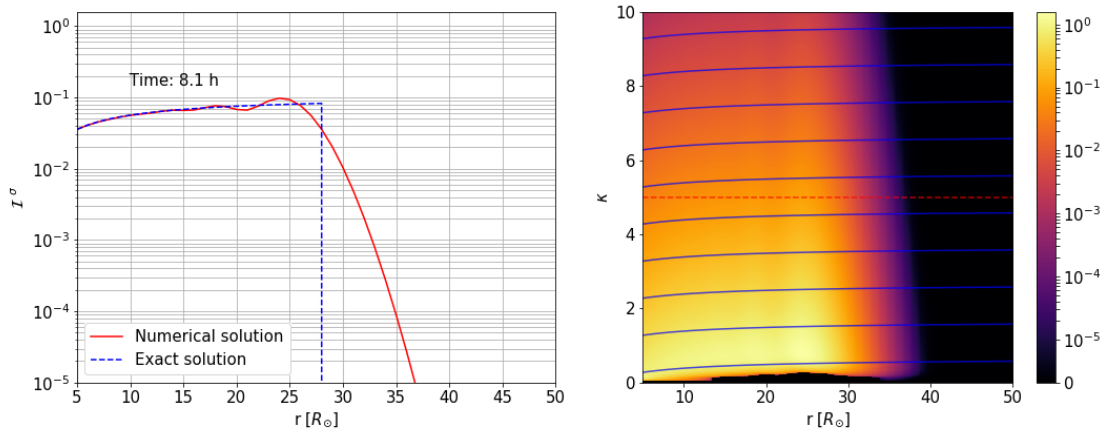

Figure 8. A conservative Lax–Wendroff simulation at the state where the analytical solution has reached approximately the halfway of the simulation box. The plot on the left contains a slice parallel to the r-axis denoted by the red dashed line in the plot on the right. The streamlines of the analytical solution are plotted as the blue lines on the plot on the right. The scaled intensity $\mathcal{I}^\sigma$ is denoted as a color gradient on the plot on the right. The simulation parameters used are $\Delta r = 1\ R_\odot$, $\Delta\kappa = 0.1$, and $\gamma = 0$

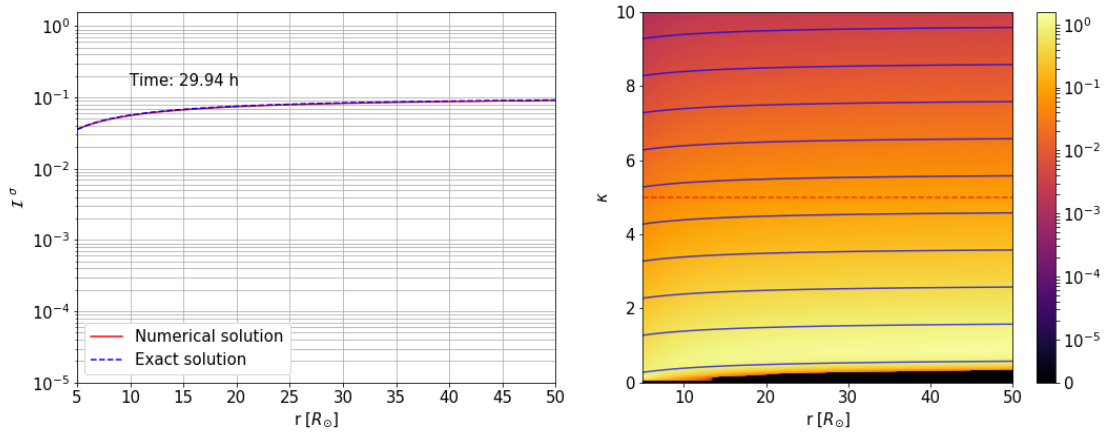

Figure 9. The steady state of the conservative Lax–Wendroff simulation presented in figure 8. The plot on the left contains a slice parallel to the r-axis denoted by the red dashed line in the plot on the right. The streamlines of the analytical solution are plotted as the blue lines on the plot on the right. The scaled intensity $\mathcal{I}^\sigma$ is denoted as a color gradient on the plot on the right. The simulation parameters used are $\Delta r = 1\ R_\odot$, $\Delta\kappa = 0.1$, and $\gamma = 0$

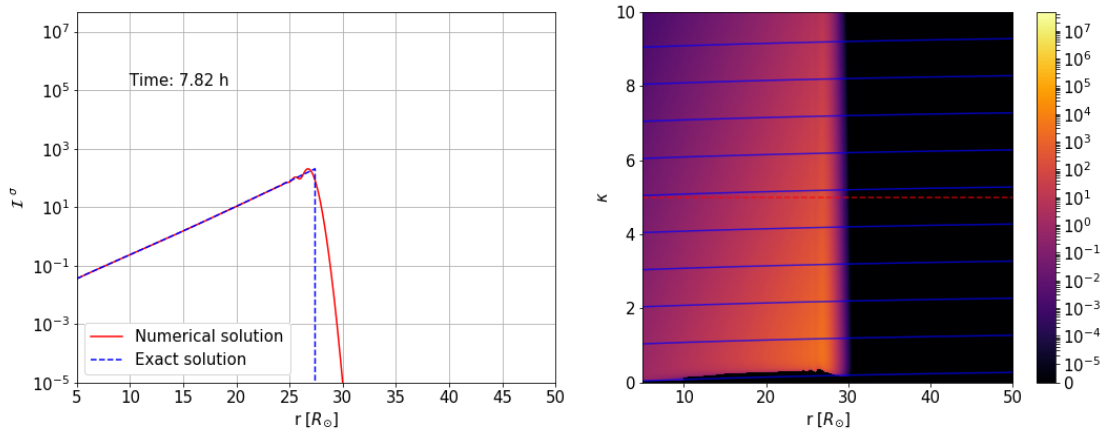

Figure 10. A conservative Lax–Wendroff simulation at the state where the analytical solution has reached approximately the halfway of the simulation box. The plot on the left contains a slice parallel to the r-axis denoted by the red dashed line in the plot on the right. The streamlines of the analytical solution are plotted as the blue lines on the plot on the right. The scaled intensity $\mathcal{I}^\sigma$ is denoted as a color gradient on the plot on the right. The simulation parameters used are $\Delta r = 0.1\ R_\odot$, $\Delta\kappa = 0.1$, and $\gamma = 1$

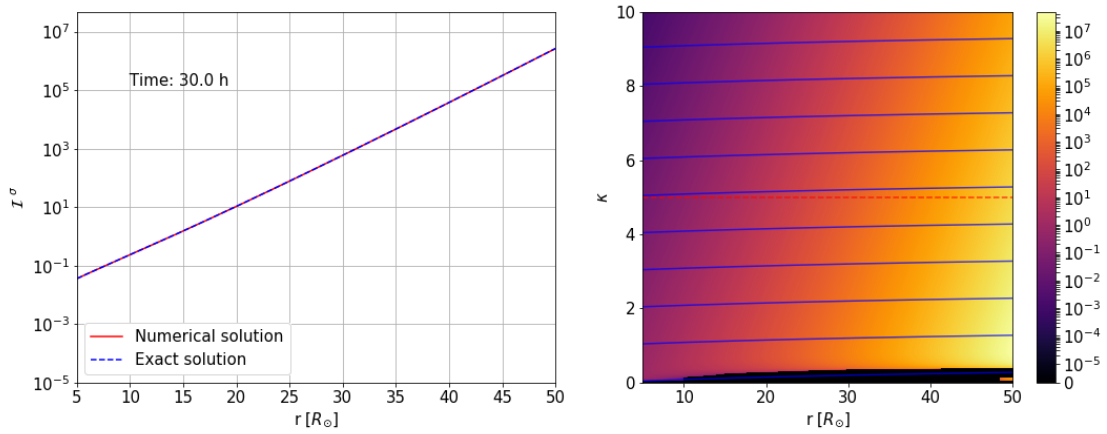

Figure 11. The steady state of the conservative Lax–Wendroff simulation presented in figure 10. The plot on the left contains a slice parallel to the r-axis denoted by the red dashed line in the plot on the right. The streamlines of the analytical solution are plotted as the blue lines on the plot on the right. The scaled intensity $\mathcal{I}^\sigma$ is denoted as a color gradient on the plot on the right. The simulation parameters used are $\Delta r = 0.1\ R_\odot$, $\Delta\kappa = 0.1$, and $\gamma = 1$

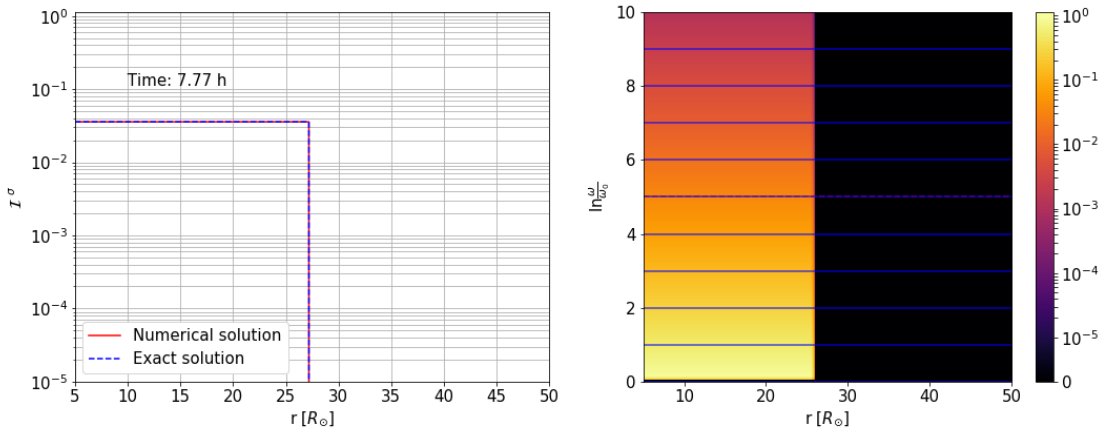

Figure 12. A semi-Lagrangian simulation at the state where the analytical solution has reached approximately the halfway of the simulation box. The plot on the left contains a slice parallel to the r-axis from the level $w = 5$. The streamlines of the analytical solution are plotted as the blue lines on the plot on the right. The scaled intensity $\mathcal{I}^\sigma$ is denoted as a color gradient on the plot on the right. The simulation parameters used are $\Delta r_0 = 0.5\ R_\odot$, $\Delta\omega = 0.1$, and $\gamma = 0$

analytical simulation settings.

2.3.5 Resolution Refiner

The variable resolution allowed by the Resolution Refiner can be used when dealing with variable conditions in simulations with areas requiring extra precision, e.g. big gradients, and can be used to significantly cut the simulation time when needed and optimized well.

The simulation results of a split and merge test are presented in figures 16, 17, and 18, where, in order to highlight the resolution changes, the scaled intensity domain is more limited. The simulation starts as a normal semi-Lagrangian simulation (figure 16). For demonstration purposes the cells in a small area are first merged to from bigger cells (figure 17), which can be detected as a granulation in the plot on the right, and then split again back to the original sizes (figure 18). The simulation's solution stays identical in a dynamic and steady state as the splitting and merging shouldn't affect the results at all.

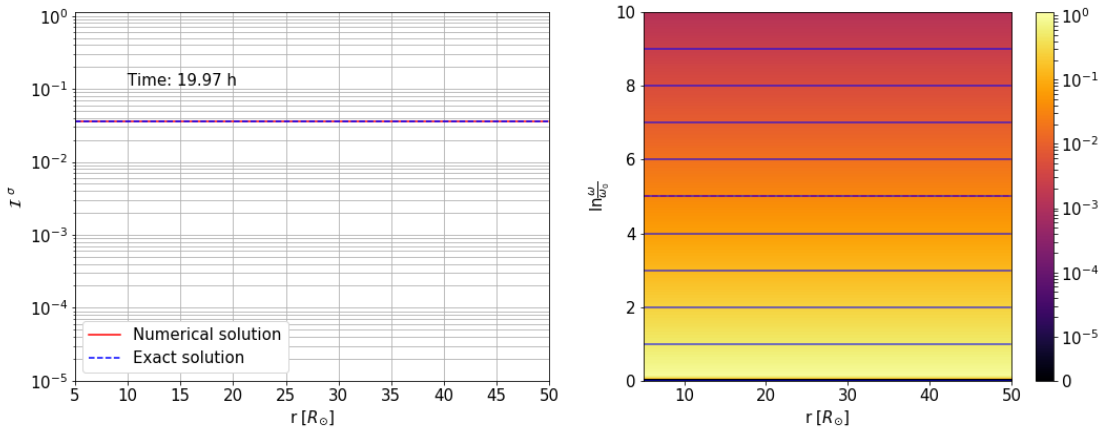

Figure 13. The steady state of the semi-Lagrangian simulation presented in figure 12. The plot on the left contains a slice parallel to the r-axis from the level $w = 5$. The streamlines of the analytical solution are plotted as the blue lines on the plot on the right. The scaled intensity $\mathcal{I}^\sigma$ is denoted as a color gradient on the plot on the right. The simulation parameters used are $\Delta r_0 = 0.5\ R_\odot$, $\Delta\omega = 0.1$, and $\gamma = 0$

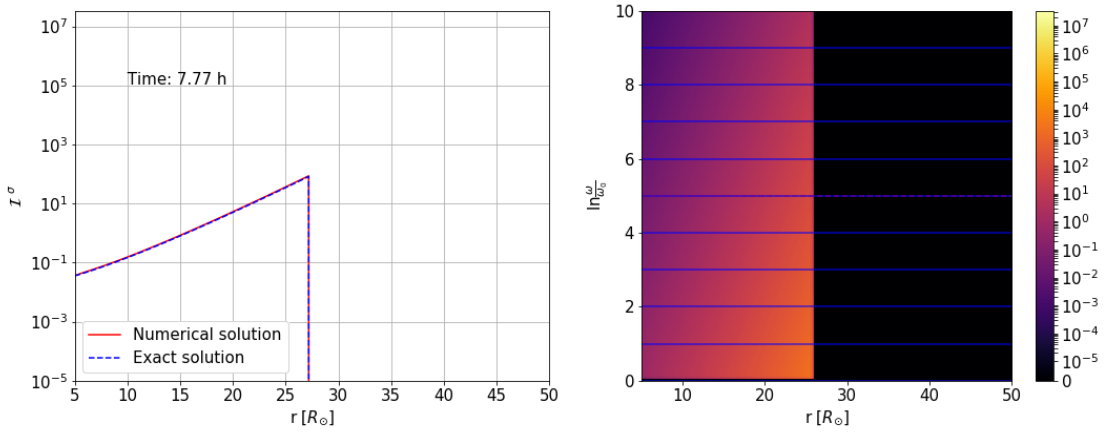

Figure 14. A semi-Lagrangian simulation at the state where the analytical solution has reached approximately the halfway of the simulation box. The plot on the left contains a slice parallel to the r-axis from the level $w = 5$. The streamlines of the analytical solution are plotted as the blue lines on the plot on the right. The scaled intensity $\mathcal{I}^\sigma$ is denoted as a color gradient on the plot on the right. The simulation parameters used are $\Delta r_0 = 0.5\ R_\odot$, $\Delta\omega = 0.1$, and $\gamma = 1$

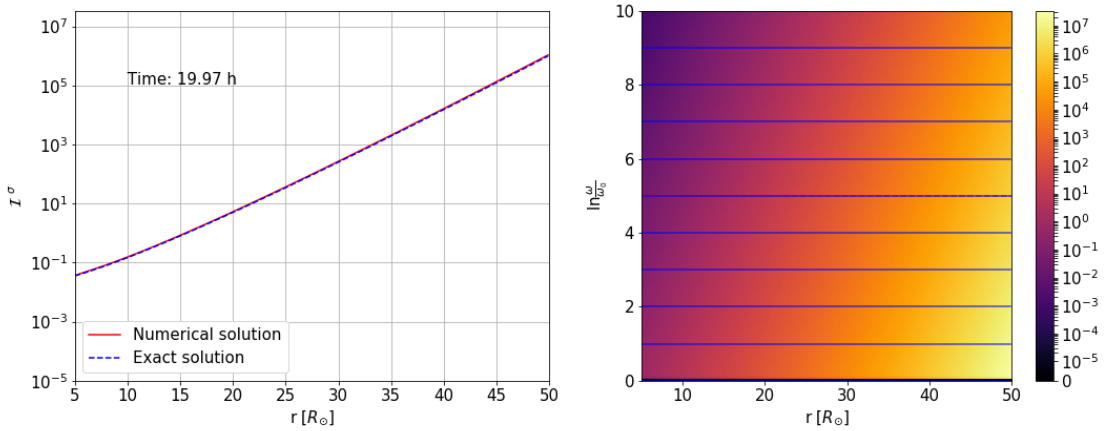

Figure 15. The steady state of the semi-Lagrangian simulation presented in figure 14. The plot on the left contains a slice parallel to the r-axis from the level $w = 5$. The streamlines of the analytical solution are plotted as the blue lines on the plot on the right. The scaled intensity $\mathcal{I}^\sigma$ is denoted as a color gradient on the plot on the right. The simulation parameters used are $\Delta r_0 = 0.5\ R_\odot$, $\Delta\omega = 0.1$, and $\gamma = 1$

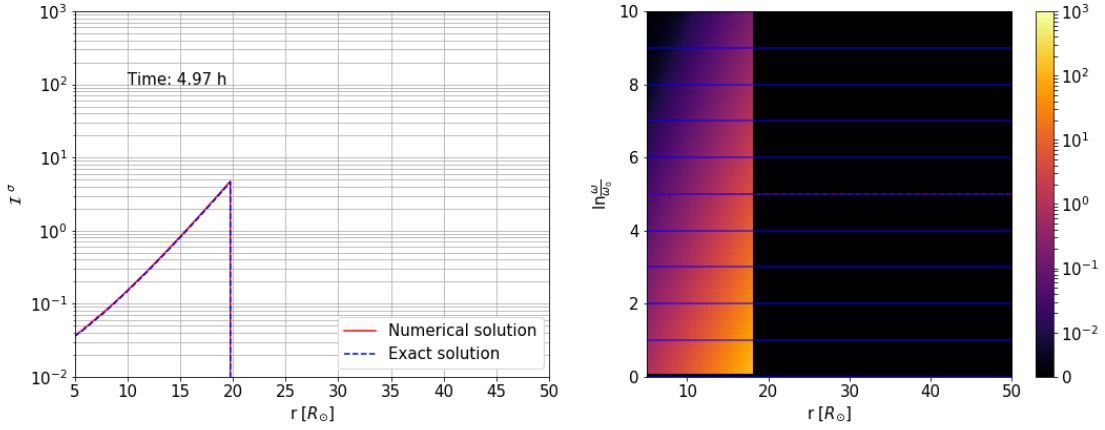

Figure 16. A semi-Lagrangian simulation with resolution refinement implemented at the state right before cell merging. The plot on the left contains a slice parallel to the r-axis from the level $w = 5$. The streamlines of the analytical solution are plotted as the blue lines on the plot on the right. The scaled intensity $\mathcal{I}^\sigma$ is denoted as a color gradient on the plot on the right. The simulation parameters used are $\Delta r_0 = 0.5\ R_\odot$, $\Delta\omega = 0.1$, and $\gamma = 1$

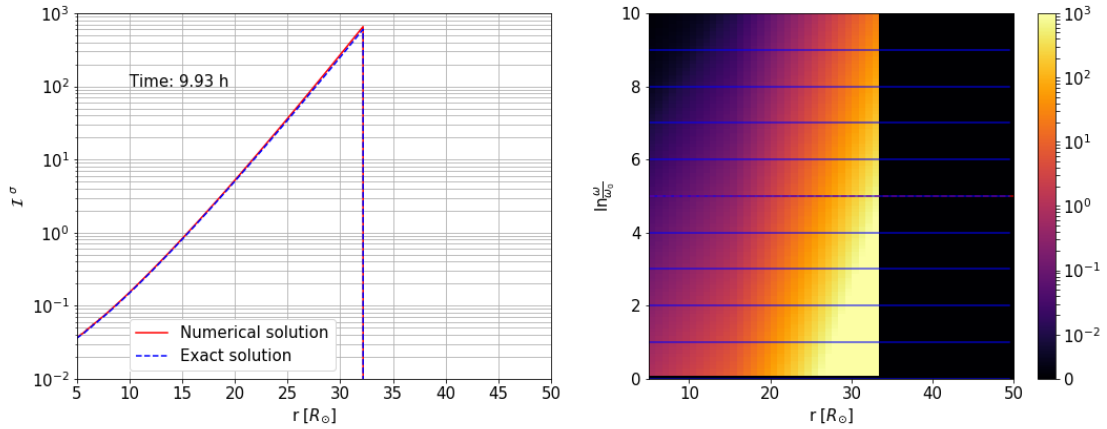

Figure 17. A semi-Lagrangian simulation with resolution refinement implemented at a state after cell merging, right before cell splitting. Comparing the plot on the right to the plot in figure 16 some granulation can be detected as vertical lines. The plot on the left contains a slice parallel to the r-axis from the level $w = 5$. The streamlines of the analytical solution are plotted as the blue lines on the plot on the right. The scaled intensity $\mathcal{I}^\sigma$ is denoted as a color gradient on the plot on the right. The simulation parameters used are $\Delta r_0 = 0.5\ R_\odot$, $\Delta\omega = 0.1$, and $\gamma = 1$

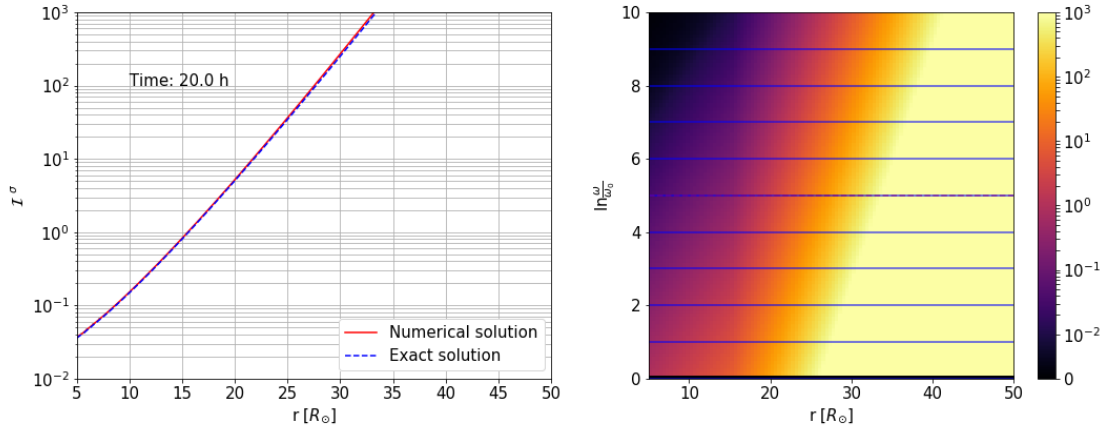

Figure 18. A semi-Lagrangian simulation with resolution refinement implemented at a state after cell splitting. Comparing the plot on the right to the plot in figure 17 the granulation has smoothed out, as expected. The plot on the left contains a slice parallel to the r-axis from the level $w = 5$. The streamlines of the analytical solution are plotted as the blue lines on the plot on the right. The scaled intensity $\mathcal{I}^\sigma$ is denoted as a color gradient on the plot on the right. The simulation parameters used are $\Delta r_0 = 0.5\ R_\odot$, $\Delta\omega = 0.1$, and $\gamma = 1$

2.4 Discussion

The semi-Lagrangian scheme is the most promising of the methods described to simulate wave evolution in an interplanetary space environment. The non-conservative and conservative upwind schemes, and the conservative Lax–Wendroff scheme were also found to be successful in solving the steady state of the system, albeit their usual requirement of fine resolutions leading to higher computation times. The conservative Lax–Wendroff scheme can be considered as a great alternative to the semi-Lagrangian scheme if the simulation setting requires a time dependent velocity field, as this would require additional implementations to the grid solver in the semi-Lagrangian scheme.

The scaled spectral magnetic intensity $\mathbb{I}^\sigma$ that was presented in section 2.2.3 could be used in the non-conservative schemes to simplify the growth term. However, the scaling implemented in the non-conservative equations usefully demonstrates the non-conservative methods' performance with an r-dependent growth factor.

Discrepancies between exact and simulated results may be caused by numerical inaccuracies leading to inaccurate wave growth evaluation and diffusion. These problems could be tackled with finer resolutions or wave transport and growth implementations that would conserve the wave energy of the system better.

As we now have a working base to simulate WKB transport we could use it to simulate situations, where there is no analytical solution. While the development of such methodology was one of the main objectives of this thesis, the exploration of such cases is out of its scope.

3 Three-wave Interactions in Coronal Loops

Coronal loops are magnetic field structures on the surface of the Sun, where the magnetic field lines start and end in different locations on the surface. Coronal loops

vary immensely in lengths ranging from tens to tens of thousands of kilometers, with bigger magnetic loops extending even further beyond. Both ends of the loop inject waves to the field line, which leads us to a situation where counter-propagating waves are present in the plasma. Thus, in addition to wave growth, wave-wave interactions need to be simulated. [7]

3.1 Theoretical Background

The model used in this thesis is based on three-wave interaction models described originally by Chin & Wentzel [34] and Wentzel [35] and used in Vainio & Spanier [36]. The three-wave interaction model consists of two Alfvén waves and a sound wave interacting. Low plasma β and high plasma β have different physics for this interaction, but in this thesis only the low plasma β physics is covered, where the sound speed is significantly smaller than the Alfvén speed. This applies in most of the corona and inner solar wind.

In low β plasma it is possible for an Alfvén wave to decay to an Alfvén wave moving in the opposite direction and a sound wave moving in the same direction. The reaction can happen both ways, so a sound wave can interact with an oncoming Alfvén wave to generate a new Alfvén wave. These reactions require that the resonance conditions

$$\begin{aligned} \omega_A^{\pm} &= \omega_A^{\mp} + \omega_S^{\pm} \\ k_A^{\pm} &= k_A^{\mp} + k_S^{\pm}, \end{aligned} \tag{44}$$

where A denotes Alfvén waves and S denotes sound waves, and $\omega_A^{\pm} = \pm k_A^{\pm} v_A$ and $\omega_S^{\pm} = \pm k_S^{\pm} c_S$, are fulfilled.

In addition to wave-wave interactions between Alfvén waves and sound waves, Alfvén waves propagating (nearly) perpendicular to the magnetic field in opposite directions can interact with each other, causing cascades of energy to higher wavenumbers. These resulting cascades can be thought of as Alfvén waves propa-

gating through the wave number space while interacting with zero-frequency Alfvén waves; thus, the wave-number transport is in the direction perpendicular to the magnetic field. Alfvén-wave cascades were originally described by Iroshnikov [37] and Kraichnan [38] and later redescribed notably by Verma [39]. These interactions between Alfvén waves are usually replaced in modeling by ad hoc equations that in wave-wave interactions allow the waves to move in k-space, e.g. by diffusion [40]. Three-wave interactions of dispersive plasma waves have been studied in [41].

As particles propagate through the magnetized plasma, they are susceptible to interactions with waves, due to their gyro motion [5]. A *wave-particle interaction* between Alfvén waves and ions is considered to be a constituent in high coronal ion temperature and high solar wind speeds [15]. For the *pitch angle scattering* to be a relevant process of particle from the thermal pool, the wave power spectrum needs to be intense enough at the ion cyclotron frequency range [16]. Pitch angle scattering off lower frequency Alfvén waves is critical for *diffusive shock acceleration*, which is currently the preferred particle acceleration mechanism [36, 42–44].

The resonance condition of a particle and an Alfvén wave requires that the particle's gyro frequency ω_c and the waves frequency ω are equal in the particle's guiding center frame of reference, which is the frame that moves along the magnetic field line with the longitudinal velocity of the particle $v_\parallel$:

$$\omega' = \omega'_c.$$

The Doppler shifted wave frequency ω' can be denoted with the frequency measured in the laboratory frame ω as

$$\omega' = \gamma_\parallel(\omega - v_\parallel k),$$

where

$$\gamma_\parallel = \frac{1}{\sqrt{1 - v_\parallel^2/c^2}}.$$

The Doppler shifted gyro frequency is defined as

$$\omega_c' = \gamma_\parallel \omega_c,$$

where ω_c is the gyro frequency in the laboratory frame of reference. The resonance condition is then

$$\omega - k v_\parallel = \omega_c, \tag{45}$$

and if the laboratory frame happens to be the plasma rest frame, the wave frequency ω can be defined as $\omega = v_A k$ and

$$k = -\frac{\omega_c}{v_\parallel - v_A}. \tag{46}$$

The resonance condition will be important in our simulation studies, as the upper limit of the frequency spectrum is defined by the dispersion relation's limits. The dispersion relation $\omega = v_A k_\parallel$ is valid only when $\omega < \omega_c$.

3.2 Numerical Methods

To simulate the effects of the wave–wave interaction we aim to simplify the simulation setting so that other effects, such as geometry, do not affect the wave distribution. The simplification of the geometrical factors can be seen in figure 19, where the curved field line is straightened out. In addition to this, we keep the Alfvén velocity constant along the field line. The employed model allows for more complex structures with easy implementation, but were not implemented due to the focus on wave–wave interactions.

The simulation still has a problem with high wave energy densities, which are partially solved by the ramp implementation described later in the boundary condition description. Other ways to combat this instability at high energy densities involve the grid resolution being altered dynamically to combat the high gradients

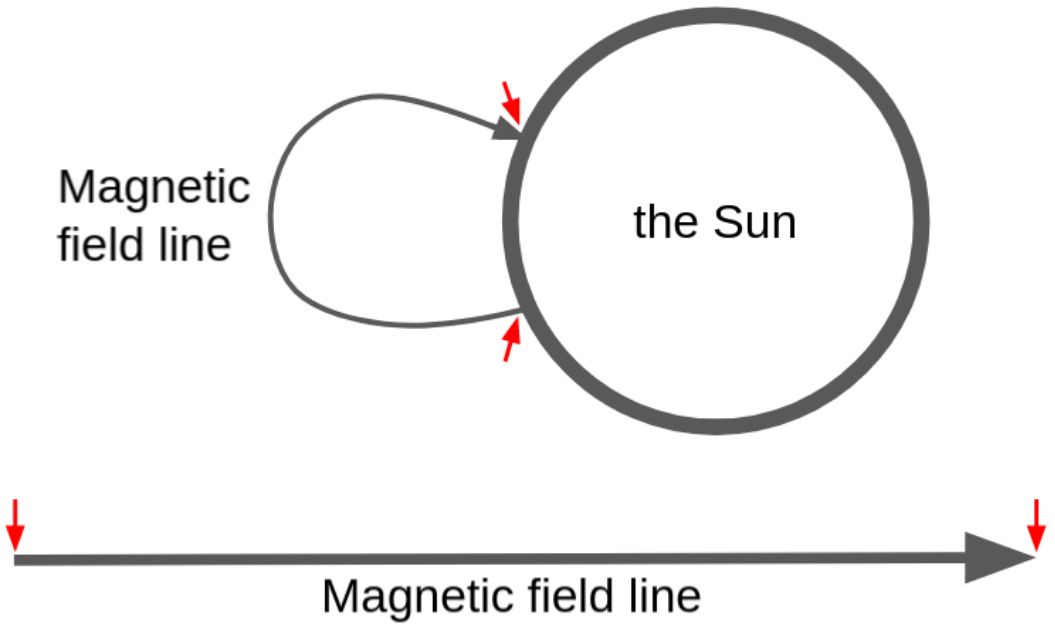

Figure 19. A depiction of the simplification of the closed field lines of the magnetic field of the Sun. The curved magnetic field line is straightened, so that geometrical factors can be ignored in the simulation. The size of the Sun and the loop are not to scale.

and growth factors present in the high energy density simulation. These were not explored in this thesis, but are noteworthy and should be investigated in the future.

The solutions presented here are explicit in time, which in itself could pose a problem for the stability of the simulation. Implicit methods, such as the Crank–Nicolson method, could help with simulating higher energy densities to really draw out the effects of wave–wave interactions.

We use a semi-Lagrangian setup, but in this setup we are observing the magnetic energy density, $\mathfrak{E}$, of the system. The wave–wave interactions of this system are described as Vainio and Spanier describe their system in [36] as what can be understood as a ladder scheme. Waves at each frequency level gain energy from oppositely propagating waves at a higher frequency level and lose energy to the oppositely propagating waves at a lower frequency level. This gives rise to the ladder-like structure that is depicted in [36], figure 1.

Instead of looking at the intensity of the waves we choose to model the wave

energy density relative to the background magnetic field energy density, since that allows for a very compact form of the governing equations. For describing energy density as a unitless quantity we further multiply it with the wavenumber as was done in [36]:

$$\mathfrak{E}^{\pm} = k|\omega^{\pm}|N_A^{\pm}/U_B, \tag{47}$$

where k is the wave number, $|\omega^{\pm}|$ the wave frequency of the respective direction, $N_A^{\pm}$ the wave action density of the respective direction, and U_B the background magnetic field energy density.

Including spatial transport along the magnetic field for the wave energy density as the basis for the calculations the evolution equations we want to solve read

$$\frac{\partial \mathfrak{E}^{\pm}(x,\omega_j,t)}{\partial t} \pm v_A \frac{\partial \mathfrak{E}^{\pm}(x,\omega_j,t)}{\partial x} = \Gamma^{\pm}(x,\omega_j,t)\mathfrak{E}^{\pm}(x,\omega_j,t), \tag{48}$$

where

$$\Gamma^{\pm}(x,\omega_j,t) = \frac{\pi\omega_j v_A^3}{c_s(v_A^2 - c_s^2)}[\mathfrak{E}^{\mp}(x,\omega_{j+1},t) - \mathfrak{E}^{\mp}(x,\omega_{j-1},t)].$$

The growth rate is dependent only on the oppositely propagating wave intensity, so the waves in this setup grow only in wave-wave interactions. This evolution equation describes Alfvén waves at frequency level $j+1$ decaying into a counter-propagating Alfvén wave at frequency level j and to a sound wave propagating in the same direction as the initial Alfvén wave. It also assumes that the sound wave will be quickly damped by the thermal plasma, and therefore the wave frequency evolution occurs in one direction, i.e., from higher to lower frequencies, only.

The resolution of the ω-axis is defined by

$$\omega_j = \omega_{j-1}\frac{v_A + c_s}{v_A - c_s}, \tag{49}$$

$$\omega_0 = 10 \cdot \frac{2\pi v_A}{\Delta x}, \tag{50}$$

where Δx is the length of the spatial cell, so that each spatial cell fits at least 10 waves at the lowest frequency.

The time resolution of the system is defined simply as

$$\Delta t = \frac{\Delta x}{v_A} \tag{51}$$

due to our choice of a constant Alfvén velocity, leaving the semi-Lagrangian grid equispaced.

The parameters chosen for the system are

$$\begin{aligned} v_A &= 1932.5 \text{ km/s} = 10 \ R_\odot/\text{h} \\ c_S &= 386.5 \text{ km/s} = 2 \ R_\odot/\text{h} \\ x &\in [0, L], \quad L = 10000 \text{ km} \\ \omega &\in [\omega_0, 3 \cdot 10^6 \ 1/\text{s}], \end{aligned}$$

where the values of the Alfvén velocity and sound speed are chosen as usual coronal parameters, L as the size of a small magnetic loop, the lower limit of ω as ω_0 defined earlier in equation (50), and the upper limit of ω as the proton cyclotron frequency corresponding to a magnetic field of about 0.03 T.

If we assume that the magnetic field B of the loop depends inversely on the loop's length L,

$$B \propto \frac{1}{L},$$

and then assume that the product BL is constant, we come to the conclusion that, although this is a relatively small magnetic loop, the simulation scales so that results for bigger loops would be qualitatively similar.

The limiting of the angular frequency domain to the ion cyclotron frequency also considerably lessens the numerical instabilities in the simulation, as the high frequency end is unstable at high energy densities. The simulation still has a problem with high energy densities, as high energy densities result in huge values of the growth factor, leading to instabilities.

The evolution equation (48) is then cast to the LOD-equivalent scheme used in the simulation:

$$\begin{aligned}&\mathfrak{E}^{\pm}(x_i,\omega_j,t+\Delta t)\\&=\mathfrak{E}^{\pm}(x_{i\mp1},\omega_j,t)\cdot\exp\left[\frac{\Delta t\pi\omega_j v_A^3}{c_S(v_A^2-c_s^2)}[\mathfrak{E}^{\mp}(x_{i\pm1},\omega_{j+1},t)-\mathfrak{E}^{\mp}(x_{i\pm1},\omega_{j-1},t)]\right].\end{aligned}\tag{52}$$

The boundaries of the angular frequency domain are treated differently due to the missing cells beyond the borders. Here we have chosen to extrapolate the energy density values from the neighboring cell by choosing a constant spectral index δ for the border. For the lower limit the value is calculated as

$$\mathfrak{E}^{\pm}(x,\omega_0,t)=\mathfrak{E}^{\pm}(x,\omega_1,t)\left(\frac{\omega_0}{\omega_1}\right)^{\delta},\quad \delta=-1.5\tag{53}$$

and the upper limit as

$$\mathfrak{E}^{\pm}(x,\omega_N,t)=\mathfrak{E}^{\pm}(x,\omega_{N-1},t)\left(\frac{\omega_N}{\omega_{N-1}}\right)^{\delta},\quad \delta=-1.\tag{54}$$

This might cause unconventional behavior close to the borders, which should be taken into account when analyzing the spectra.

3.3 Results

3.3.1 Power-law Injection

The original idea was to inject wave intensity as a power law as was done in [36], but was altered to combat the numerical instabilities due to enormous growth factors caused by huge gradients at the wave–wave interaction interface. This power law form is as follows:

$$\mathfrak{E}^{\pm}(x_0,\omega_j,t)=B\left(\frac{\omega_j}{\omega_0}\right)^{1-q},$$

where $q=5/3$ and B is a normalization parameter. This was modified so that the intensity spectrum would be injected gradually, as a *linear ramp* in time, to decrease numerical instabilities in the simulation and let wave–wave interactions

set in gradually in the simulation volume. The implementation of the linear ramp changes the injection formula to

$$\mathfrak{E}^{\pm}(x_0, \omega_j, t) = B\left(\frac{\omega_j}{\omega_0}\right)^{1-q}\left[1 - \frac{t_{ramp} - t}{t_{ramp}}\mathcal{H}(t_{ramp} - t)\right], \tag{55}$$

where $\mathcal{H}$ is the Heaviside step function, and

$$t_{ramp} = \frac{4L}{v_A}, \tag{56}$$

where L is the simulation box size in the x-direction and the multiplier of 4 is to define the ramp length to be four times the crossing time of the simulation box.

The results of the power law injection can be seen in figures 20, 21, and 22. At the halfway point in figure 20 we can see the state of the wave fronts right before bigger wave–wave interactions start happening. The subtle profile of the ramp can be distinguished in the color gradients on the right, as the intensity grows towards the injection edges. In figure 21 we can already see wave–wave interactions altering the high frequency spectrum at the far edges, where the spectrum has had time to be altered by the wave–wave interactions. The profile keeps evolving until the steady state in figure 22 where the energy of the high frequency waves has been eaten up by the interactions with the oncoming waves.

To check for the simulation's dependence on starting values, it was decided to simulate the exact same situation, but with a different size ramp. The ramp of the length $t_{ramp} = 0.5L/v_A$ was chosen to be the comparison case. The total simulation time is 45 seconds, which corresponds to about 8.7 L/v_A (depicting how many simulation box lengths the waves propagate in this time). The shorter ramp steady state is presented in figure 23. No difference is seen in the steady state solutions, leading us to believe that the simulation really solves for the steady state of the system.

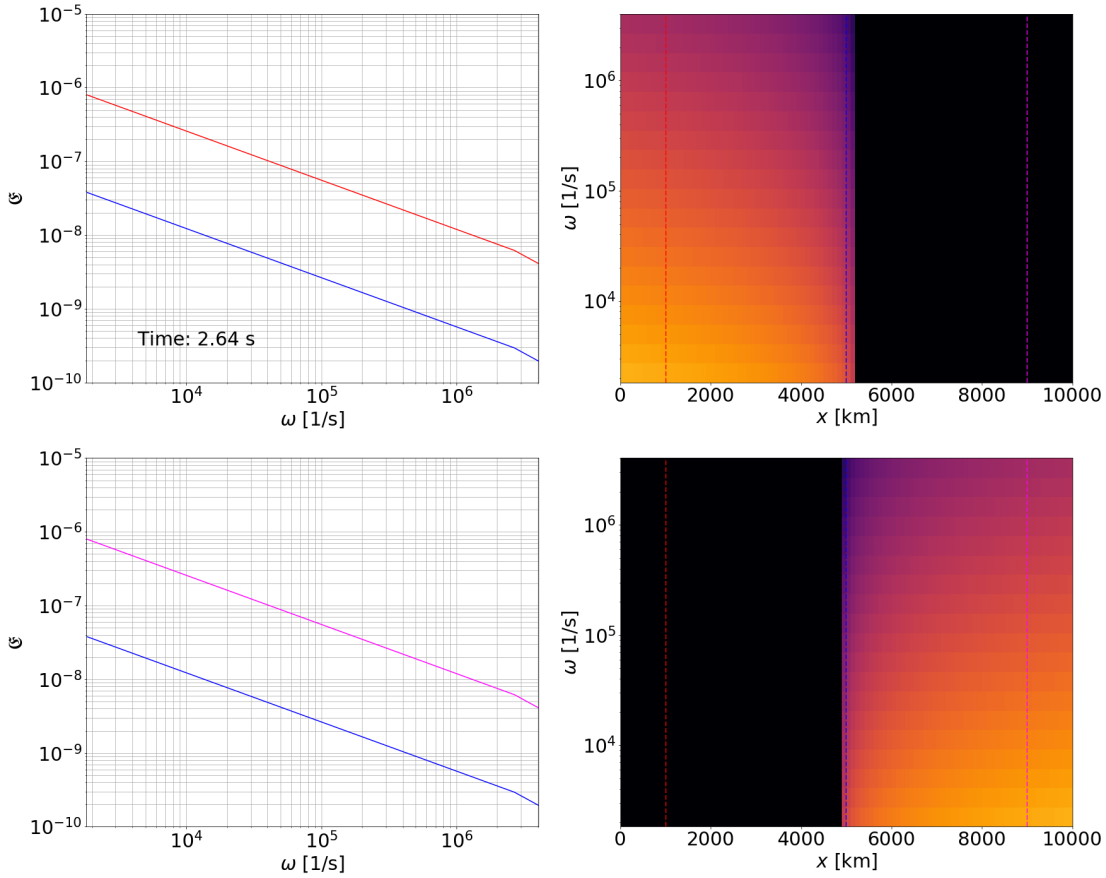

Figure 20. A semi-Lagrangian simulation of a coronal loop using a power law injection profile at the state where the wave fronts have reached approximately the halfway of the simulation box. The plots on the top row contain the forward propagating waves and the plots on the bottom row contain the backward propagating waves. The plot on the left contains color coded slices parallel to the ω-axis denoted by the colored dashed lines in the plot on the right. The normalized wave-energy density $\mathfrak{E}$ is denoted as a color gradient on the plot on the right. The simulation parameters used are $\Delta x = 100$ km and $B = 1 \cdot 10^{-5}$.

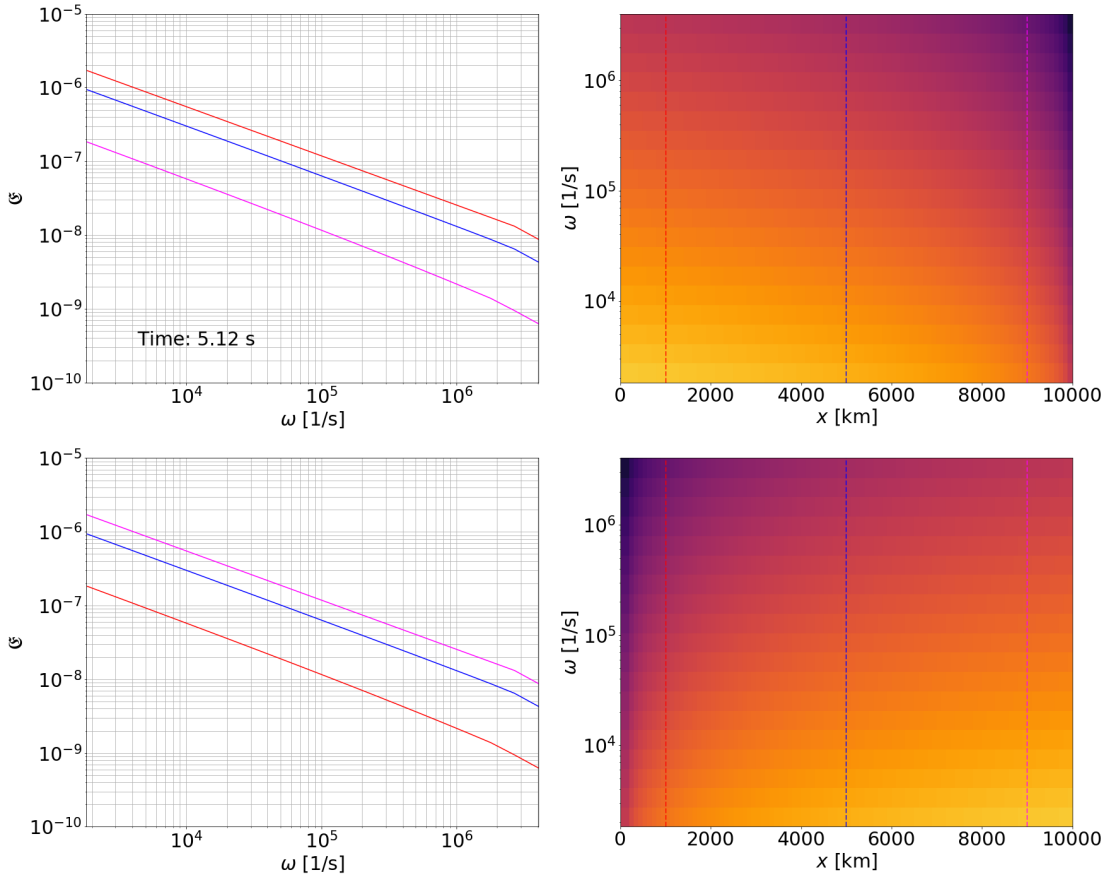

Figure 21. The semi-Lagrangian simulation of a coronal loop using a power law injection profile presented in figure 20 at the state where the wave fronts have reached the opposing end of the simulation box. The plots on the top row contain the forward propagating waves and the plots on the bottom row contain the backward propagating waves. The plot on the left contains color coded slices parallel to the ω-axis denoted by the colored dashed lines in the plot on the right. The normalized wave-energy density $\mathfrak{E}$ is denoted as a color gradient on the plot on the right. The simulation parameters used are $\Delta x = 100$ km and $B = 1 \cdot 10^{-5}$.

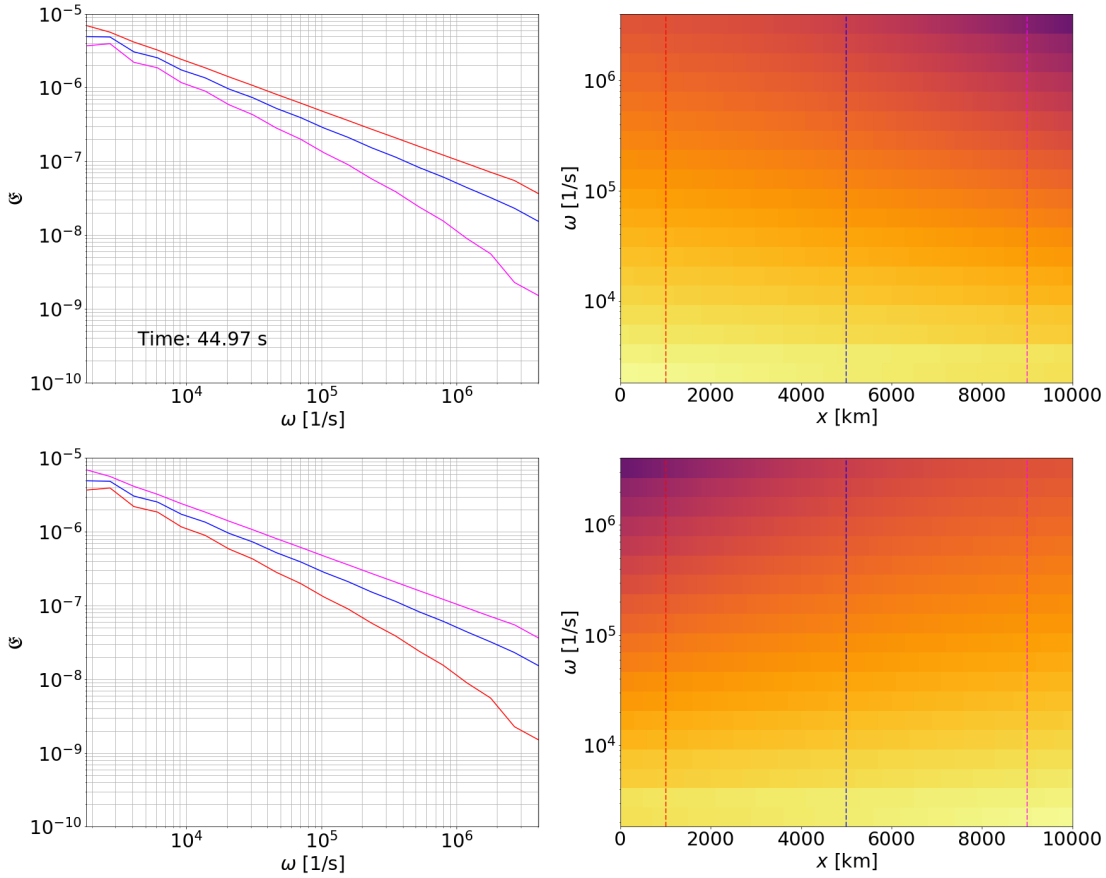

Figure 22. The steady state of the semi-Lagrangian simulation of a coronal loop using a power law injection profile presented in figures 20 and 21. The plots on the top row contain the forward propagating waves and the plots on the bottom row contain the backward propagating waves. The plot on the left contains color coded slices parallel to the ω-axis denoted by the colored dashed lines in the plot on the right. The normalized wave-energy density $\mathfrak{E}$ is denoted as a color gradient on the plot on the right. The simulation parameters used are $\Delta x = 100$ km and $B = 1 \cdot 10^{-5}$.

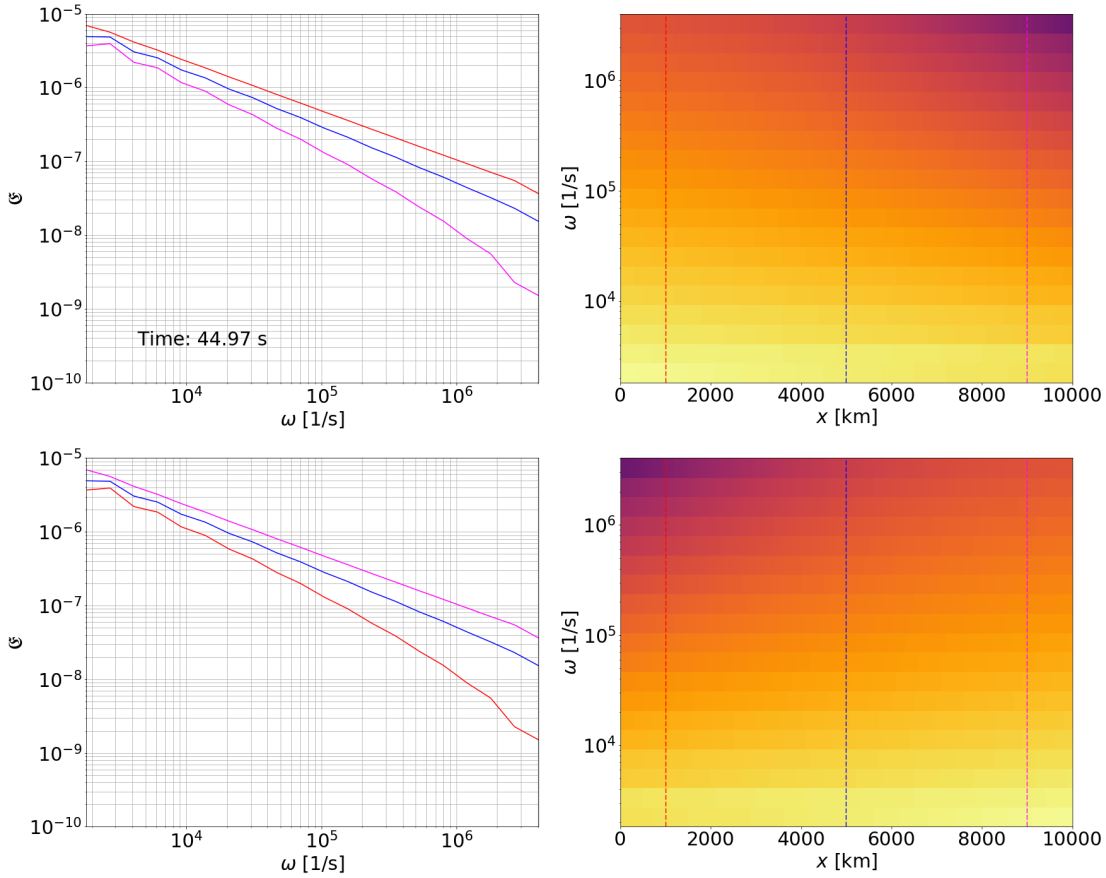

Figure 23. The steady state of a semi-Lagrangian simulation of a coronal loop using a power law injection profile with an injection ramp size of $0.5L$. The plots on the top row contain the forward propagating waves and the plots on the bottom row contain the backward propagating waves. The plot on the left contains color coded slices parallel to the ω-axis denoted by the colored dashed lines in the plot on the right. The normalized wave-energy density $\mathfrak{E}$ is denoted as a color gradient on the plot on the right. The simulation parameters used are $\Delta x = 100$ km and $B = 1 \cdot 10^{-5}$.

3.3.2 Lorentzian Peak Injection

The next profile under investigation was chosen to be a Lorentzian peak. The formulation of the peak with the injection ramp implemented as in equation (55) looks as follows:

$$\mathfrak{E}^{\pm}(x_0,\omega,t) = A\frac{2\gamma}{(\omega-\bar{\omega})^2-\gamma^2}\left[1-\frac{t_{ramp}-t}{t_{ramp}}\mathcal{H}(t_{ramp}-t)\right], \tag{57}$$

where A is a normalization parameter, γ is a chosen parameter, and $\bar{\omega}$ is the peak location. In addition, we took $\bar{\omega} = \gamma = 0.1\omega_{max}$ to fix the parameters of the simulation.

The results of the simulation can be seen in figures 24–26. The ramp development can be seen from figure 24, as the energy density of the system is lower in firstly propagated parts. As the waves start interacting with each other instabilities start to develop which can be detected in figure 25. Using a longer ramp reduces this problem as the gradients are smaller within the wave–wave interactions. The wave spectrum already starts to develop a profile in the high frequency range. At the steady state seen in figure 26 no instabilities are detected anymore. We can see that the peak that was injected is subdued very quickly after the boundary to a profile without a peak.

To check for the lost energy of the system we compared the 10 % line of figure 26 to a wave spectrum without wave-wave interactions. The comparison is presented in figure 27.

3.3.3 Lorentzian Peak Multiplied by the Angular Frequency

In addition to the earlier Lorentzian peak a second formulation was tested with the simulation, where the peak is defined as

$$\mathfrak{E}^{\pm}(x_0,\omega,t) = C\frac{2\gamma\omega}{(\omega-\bar{\omega})^2-\gamma^2}\left[1-\frac{t_{ramp}-t}{t_{ramp}}\mathcal{H}(t_{ramp}-t)\right], \tag{58}$$

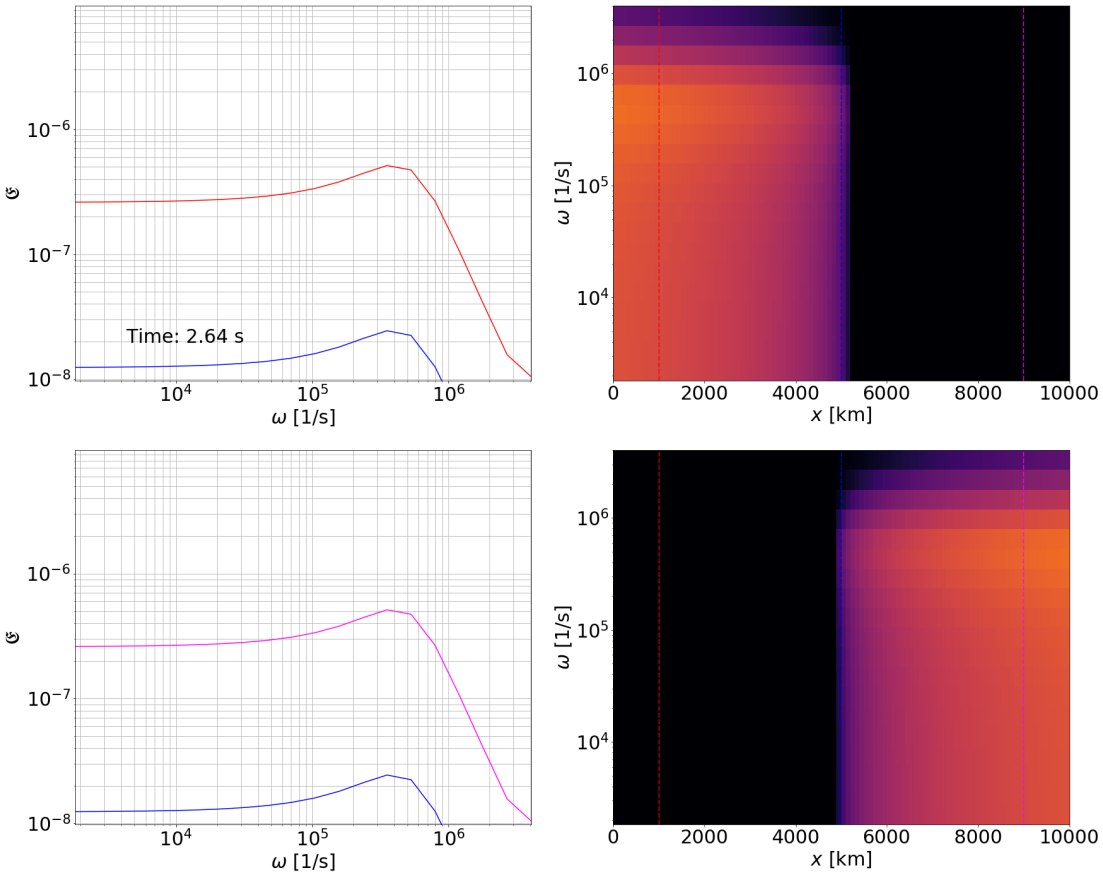

Figure 24. A semi-Lagrangian simulation of a coronal loop using a Lorentzian peak injection profile at the state where the wave fronts have reached approximately the halfway of the simulation box. The plots on the top row contain the forward propagating waves and the plots on the bottom row contain the backward propagating waves. The plot on the left contains color coded slices parallel to the ω-axis denoted by the colored dashed lines in the plot on the right. The normalized wave-energy density $\mathfrak{E}$ is denoted as a color gradient on the plot on the right. The simulation parameters used are $\Delta x = 100$ km and $A = 1$ s^{-1}.

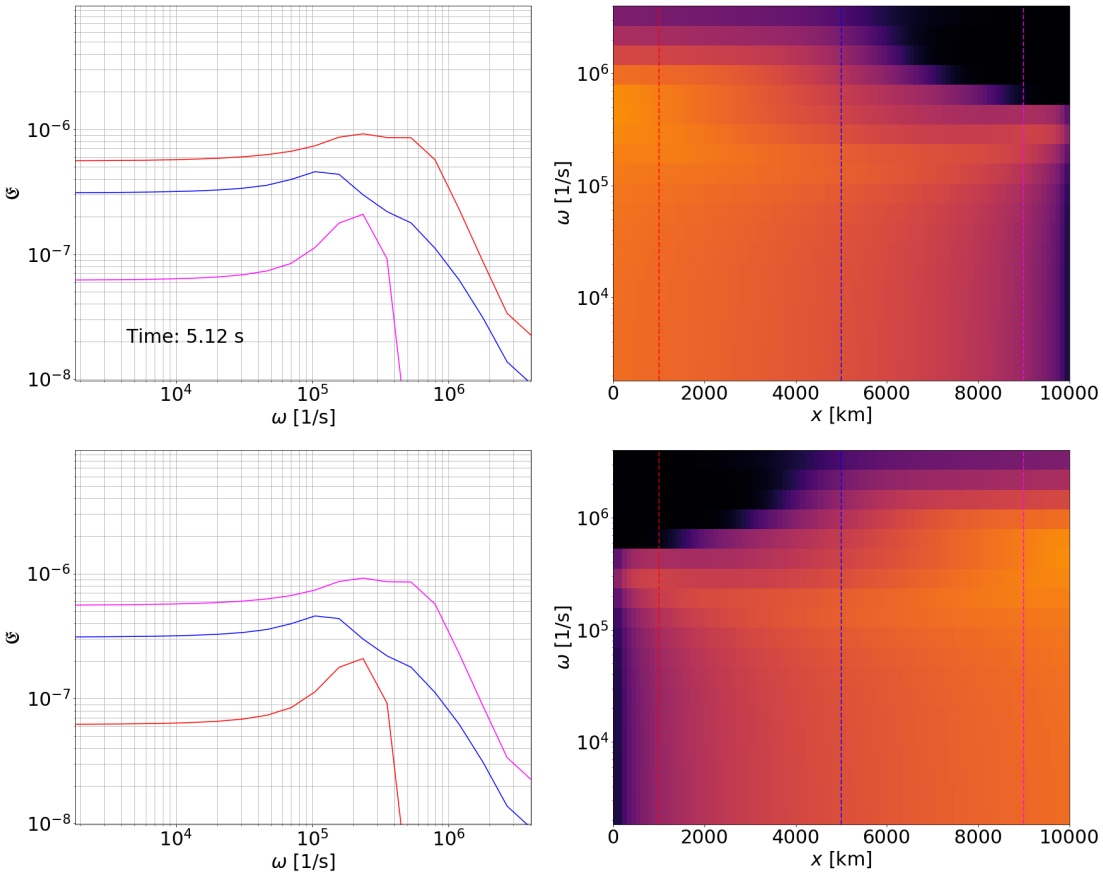

Figure 25. The semi-Lagrangian simulation of a coronal loop using a Lorentzian peak injection profile presented in figure 24 at the state where the wave fronts have reached the opposing end of the simulation box. The plots on the top row contain the forward propagating waves and the plots on the bottom row contain the backward propagating waves. The plot on the left contains color coded slices parallel to the ω-axis denoted by the colored dashed lines in the plot on the right. The normalized wave-energy density $\mathfrak{E}$ is denoted as a color gradient on the plot on the right. The simulation parameters used are $\Delta x = 100$ km and $A = 1$ s^{-1}.

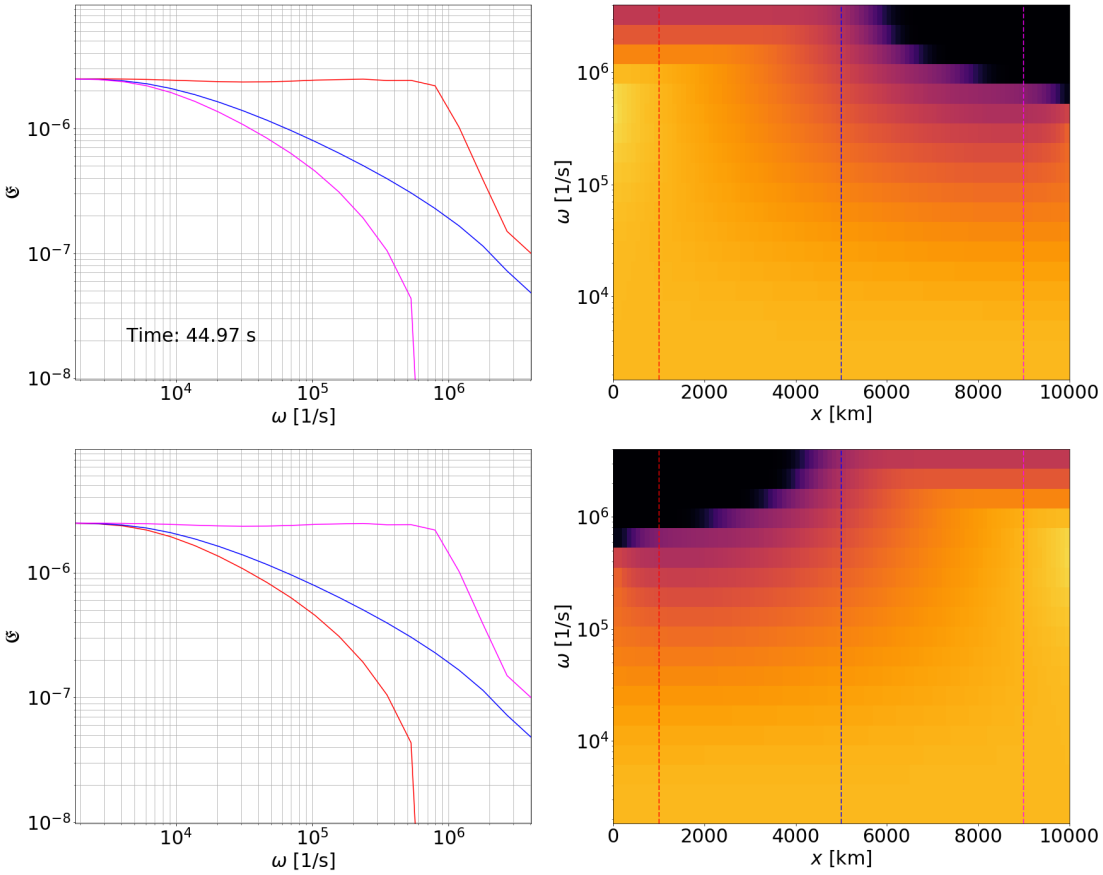

Figure 26. The steady state of the semi-Lagrangian simulation of a coronal loop using a Lorentzian peak injection profile presented in figures 24 and 25. The plots on the top row contain the forward propagating waves and the plots on the bottom row contain the backward propagating waves. The plot on the left contains color coded slices parallel to the ω-axis denoted by the colored dashed lines in the plot on the right. The normalized wave-energy density $\mathfrak{E}$ is denoted as a color gradient on the plot on the right. The simulation parameters used are $\Delta x = 100$ km and $A = 1$ s^{-1}.

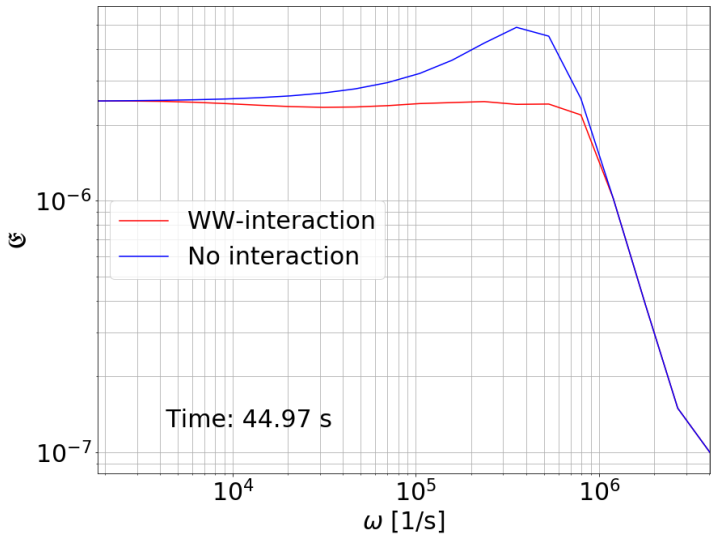

Figure 27. Steady states of semi-Lagrangian simulations of a coronal loop using a Lorentzian peak injection profile with and without wave–wave interactions at the 1000 km slice presented in figure 26. The simulation parameters used are $\Delta x = 100$ km and $A = 1$ s^{-1}.

where C is a normalization parameter, with the only differences being the factor ω in the peak and $\bar{\omega} = \gamma = 0.01\omega_{max}$.

The results can be seen in figures 28–31. The ramp can be again seen in figure 28, where the firstly injected waves are at a lower energy density than waves injected at a later time. We can again see wave–wave interactions already shaping the profile of the spectrum in figure 29, where the wave fronts first touch the end of the box. After allowing the wave spectra to evolve for a while, we can see instabilities develop in figure 30. These instabilities are more intense with higher energy density starting values, but can be contained by using a longer ramp to reduce the size of the gradients in the system. In figure 31 we can see the steady state of the system.

Analyzing the spectrum at different parts of the simulation we can estimate the spectral index $\delta = \mathrm{d}\ln\mathfrak{E}/\mathrm{d}\ln\omega$. The data is read from the forward propagation plot (top) of figure 31. Starting from the lower end of the angular frequency domain, we can see diverging of the energy densities at about $7 \cdot 10^3$ 1/s. Evaluating the spectral indices between $7 \cdot 10^3$ 1/s and $2 \cdot 10^4$ 1/s results in 1.2 for the red line, 1.5

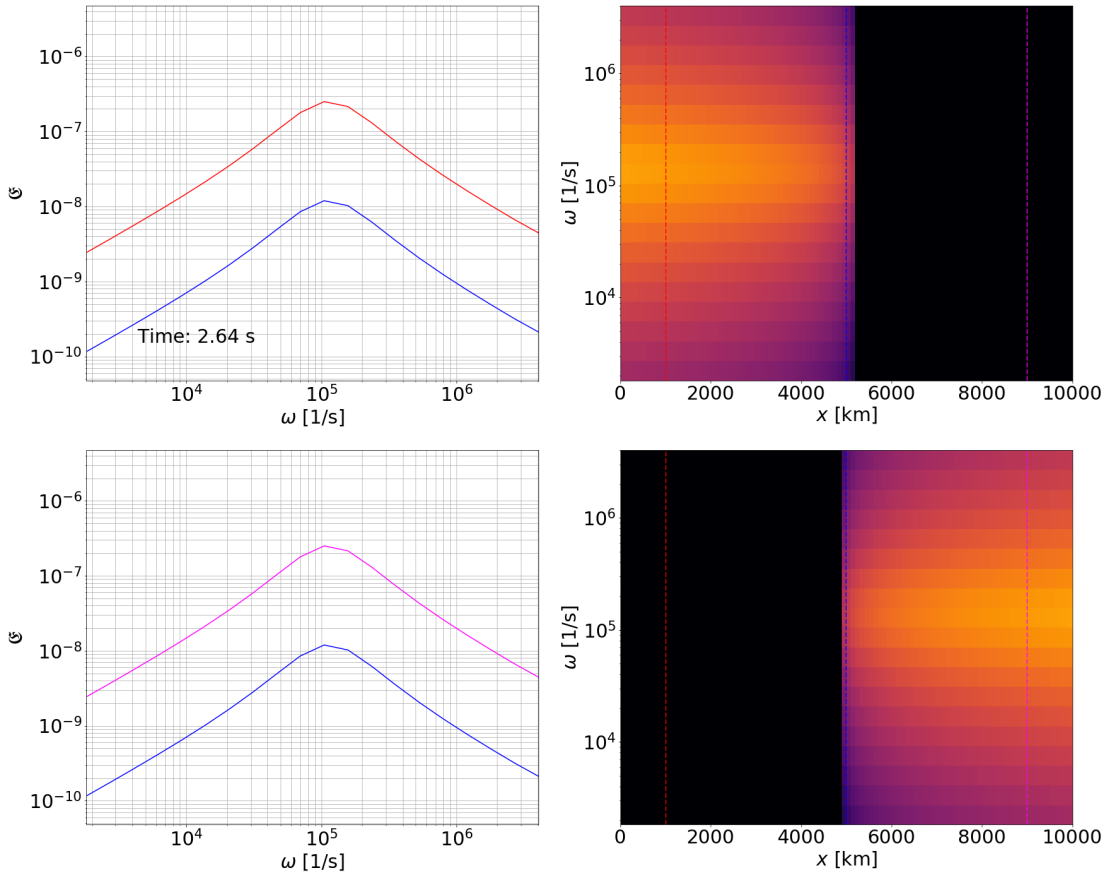

Figure 28. A semi-Lagrangian simulation of a coronal loop using a Lorentzian multiplied by ω injection profile at the state where the wave fronts have reached approximately the halfway of the simulation box. The plots on the top row contain the forward propagating waves and the plots on the bottom row contain the backward propagating waves. The plot on the left contains color coded slices parallel to the ω-axis denoted by the colored dashed lines in the plot on the right. The normalized wave-energy density $\mathfrak{E}$ is denoted as a color gradient on the plot on the right. The simulation parameters used are $\Delta x = 100$ km and $C = 1 \cdot 10^{-7}$.

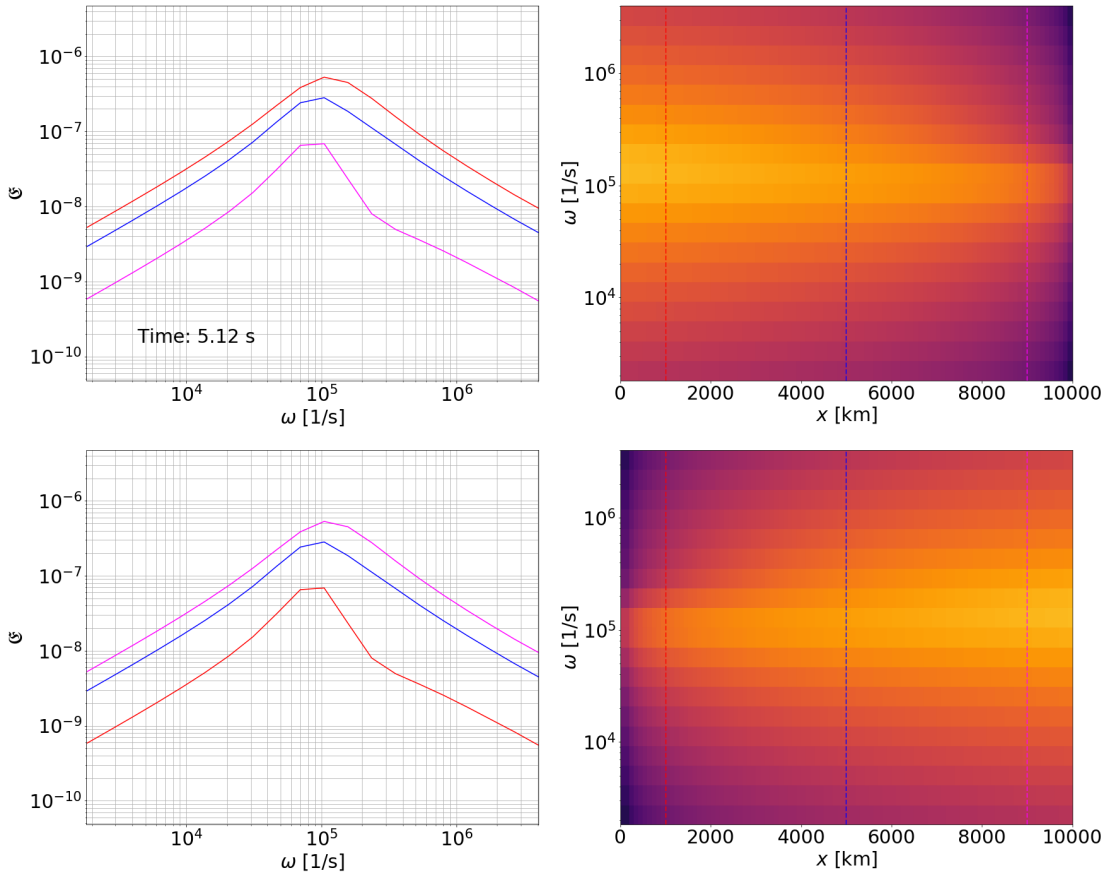

Figure 29. The semi-Lagrangian simulation of a coronal loop using a Lorentzian multiplied by ω injection profile presented in figure 28 at the state where the wave fronts have reached the opposing end of the simulation box. The plots on the top row contain the forward propagating waves and the plots on the bottom row contain the backward propagating waves. The plot on the left contains color coded slices parallel to the ω-axis denoted by the colored dashed lines in the plot on the right. The normalized wave-energy density $\mathfrak{E}$ is denoted as a color gradient on the plot on the right. The simulation parameters used are $\Delta x = 100$ km and $C = 1 \cdot 10^{-7}$.

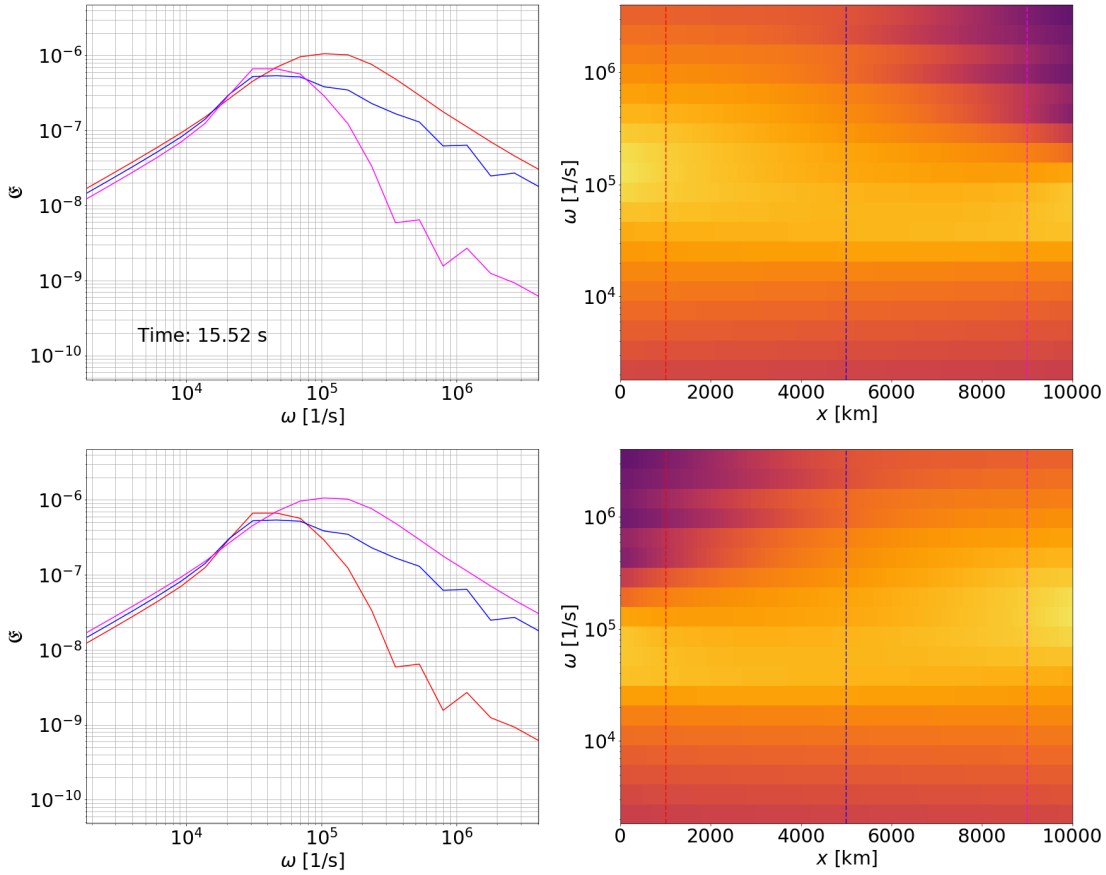

Figure 30. The semi-Lagrangian simulation of a coronal loop using a Lorentzian multiplied by ω injection profile presented in figures 28 and 29 at a state where numerical instabilities are present. The plots on the top row contain the forward propagating waves and the plots on the bottom row contain the backward propagating waves. The plot on the left contains color coded slices parallel to the ω-axis denoted by the colored dashed lines in the plot on the right. The normalized wave-energy density $\mathfrak{E}$ is denoted as a color gradient on the plot on the right. The simulation parameters used are $\Delta x = 100$ km and $C = 1 \cdot 10^{-7}$.

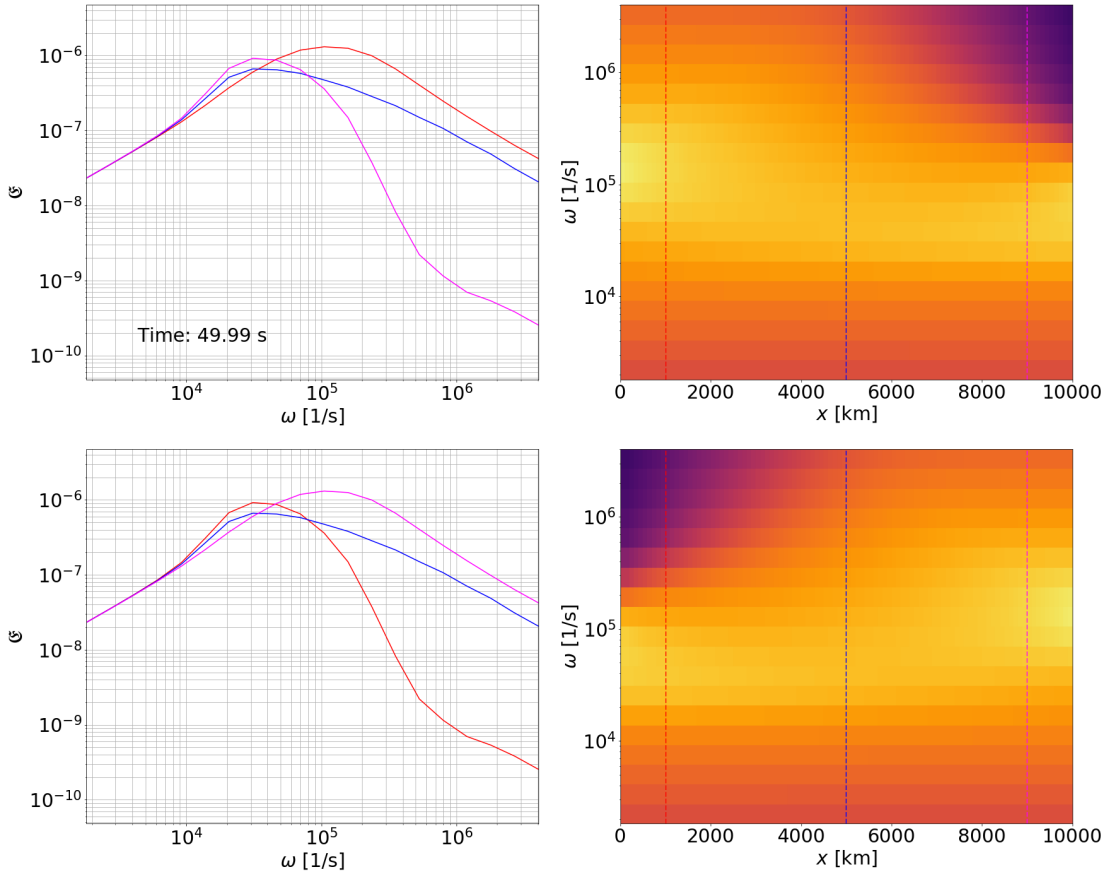

Figure 31. The steady state of the semi-Lagrangian simulation of a coronal loop using a Lorentzian multiplied by ω injection profile presented in figures 28, 29, and 30. The plots on the top row contain the forward propagating waves and the plots on the bottom row contain the backward propagating waves. The plot on the left contains color coded slices parallel to the ω-axis denoted by the colored dashed lines in the plot on the right. The normalized wave-energy density $\mathfrak{E}$ is denoted as a color gradient on the plot on the right. The simulation parameters used are $\Delta x = 100$ km and $C = 1 \cdot 10^{-7}$.

for the blue line, and 1.9 for the magenta line. At this point we can also detect the shift in the peak location, from $1 \cdot 10^5$ 1/s to $2 \cdot 10^4$ 1/s. Evaluating the spectral indices after this point was conducted for the straight parts of the spectra, choosing as long of a section as possible. For the red line, δ was evaluated to be -1.1 from $3.5 \cdot 10^5$ 1/s to $3 \cdot 10^6$ 1/s, for the blue line δ was evaluated to be -0.7 from $1 \cdot 10^5$ 1/s to $5 \cdot 10^5$ 1/s, and for the magenta line δ was evaluated to be -3.3 from $1 \cdot 10^5$ 1/s to $5 \cdot 10^5$ 1/s. After their respective sections the blue and magenta line's δ converges to the δ of the red line in this area.

3.4 Discussion

The coronal loop simulations presented show effects of wave–wave interactions quite effectively. Some interesting points can already be seen in the data, with figure 23 hinting at implications towards particle transport and figure 31 showing definite spectral evolution of Alfvén waves. As such, the methods used seem to be sufficient for simulating wave transport and wave–wave interactions.

There is clearly a a single dominant wave mode at edges of the simulation box (+ at $x \approx 0$ and - at $x \approx L$). This means that close to the foot points of the coronal loop the bulk velocities of the particles that interact with the waves are pointing away from the surface of the Sun.Because the waves at the opposite sides of the loop are propagating towards each other, the gradient of the particles' advection velocity leads to particle acceleration.

The simulations have definite problems with the instabilities caused by large gradients of wave energy density in the system. These large gradients cause huge wave growth terms, leading to instabilities. These could be combated by finer resolutions or dynamic resolution changing discussed in section 2.3.5.

Additional wave injection spectra should be investigated to see the different effects the three-wave interactions have on the wave energy spectra. As could already

be seen in the results presented, the effects vary quite substantially depending on the injection spectra. Additionally, to drag the simulations closer to real physical situations, variable Alfvén velocities should be investigated to better simulate the environment of a coronal loop.

4 Conclusions and Outlook

A good set of simulation tools was developed to model wave transport and interactions. Upwind schemes work well as steady state solvers given their simplicity, but do not do so as dynamical solvers, due to the diffusion issue and computation time. Only the conservative Lax–Wendroff method bears the same positives as the upwind schemes, since the non-conservative scheme doesn't come close to matching the analytical solutions of the spectral intensity. The semi-Lagrangian scheme is an accurate and computationally light simulation scheme, albeit being a bit less general in its implementation compared to the other methods described.

Additionally, a tool to dynamically change the resolution of the simulation in areas needed was developed to really cut down on otherwise large simulation times. This tool can prove to be useful in many kinds of grid simulation settings, and should be taken into account when developing large simulations.

The coronal loop simulations give insight into the spectra created by wave–wave interactions, and even hints of implications for particle transport. These simulations are not as stable in their current form as desired, but can be significantly improved with the resolution refiner developed and the ramp implementation used.

The simulation methods and results of this thesis can be used to have more accurate representations of Alfvén wave spectra in other kinds of interplanetary constituent simulations, e.g. particle acceleration and shock wave simulations. The wave solvers created also work on other kinds of wave quanta entirely, with the implementation of the respective physical equations of the systems investigated.

References

[1] Afanasiev, A. N., Kocharov, L. G., & Vainio, R. O. (2011). Stochastic Re-Acceleration of Protons in the Downstream Region of a Coronal Shock. AGUFM, 2011, SH34A-02. https://ui.adsabs.harvard.edu/abs/2011AGUFMSH34A..02A/abstract

[2] Afanasiev, A., & Vainio, R. (2013). Monte carlo simulation model of energetic proton transport through self-generated alfvén waves. Astrophysical Journal, Supplement Series, 207(2). https://doi.org/10.1088/0067-0049/207/2/29

[3] Afanasiev, A., Vainio, R., & Kocharov, L. (2014). The effect of stochastic reacceleration on the energy spectrum of shock-accelerated protons. Astrophysical Journal, 790(1). https://doi.org/10.1088/0004-637X/790/1/36

[4] Afanasiev, A. N., Vainio, R. O., & Battarbee, M. C. (2014). The Form of Proton Energy Spectra from Self-Consistent Simulations of the Coronal Shock Acceleration. American Geophysical Union, Fall Meeting 2014, Abstract Id.SH21B-4104, 2014, SH21B-4104. https://ui.adsabs.harvard.edu/abs/2014AGUFMSH21B4104A/abstract

[5] Koskinen, H. (2011). Physics of Space Storms: From the Solar Surface to the Earth. Springer. https://doi.org/10.1007/978-3-642-00319-6

[6] Hale, G. E. (1908). On the Probable Existence of a Magnetic Field in Sun-Spots. The Astrophysical Journal, 28, 315. https://doi.org/10.1086/141602

[7] Aschwanden, M. J. (2005). Physics of the Solar Corona. An Introduction with Problems and Solutions (2nd edition). Springer. Retrieved from https://ui.adsabs.harvard.edu/abs/2005psci.book.....A/abstract

[8] Biermann, L. (1957). Solar corpuscular radiation and the interplanetary gas. The Observatory (Vol. 77). Retrieved from https://ui.adsabs.harvard.edu/abs/1957Obs....77..109B/abstract

[9] Biermann, L. (1951). Kometenschweife und solare Korpuskularstrahlung. Zeitschrift für Astrophysik, Vol. 29, p.274 (Vol. 29). Retrieved from https://ui.adsabs.harvard.edu/abs/1951ZA.....29..274B/abstract

[10] Alfvén, H. (1957). On the Theory of Comet Tails. Tellus, 9(1), 92–96. https://doi.org/10.1111/j.2153-3490.1957.tb01855.x

[11] Parker, E. N. (1958). Dynamics of the Interplanetary Gas and Magnetic Fields. The Astrophysical Journal, 128, 664. https://doi.org/10.1086/146579

[12] Kilpua, E., & Koskinen, H. (2017). Introduction to Plasma Physics. University of Helsinki, Department of Physics: Limes ry.

[13] Alfvén, H. (1942). Existence of electromagnetic-hydrodynamic waves. In Nature (Vol. 150, Issue 3805, pp. 405–406). https://doi.org/10.1038/150405d0

[14] Ng, C. K., Reames, D. V., & Tylka, A. J. (2003). Modeling Shock-accelerated Solar Energetic Particles Coupled to Interplanetary Alfvén Waves. The Astrophysical Journal, 591(1), 461–485. https://doi.org/10.1086/375293

[15] Vainio, R., & Laitinen, T. (2001). The relation between cyclotron heating and energetic particles on open coronal field lines. Astronomy and Astrophysics, 371(2), 738–747. https://doi.org/10.1051/0004-6361:20010411

[16] Laitinen, T., Fichtner, H., & Vainio, R. (2003). Toward a self-consistent treatment of the cyclotron wave heating and acceleration of the solar wind plasma. Journal of Geophysical Research: Space Physics, 108(A2). https://doi.org/10.1029/2002JA009479

[17] Laitinen, T., & Vainio, R. (2003). Shock acceleration of energetic particles in wave heated corona. Advances in Space Research, 32(12), 2603–2608. https://doi.org/10.1016/S0273-1177(03)00932-3

[18] Hollweg, J. V. (1974). Transverse Alfvén waves in the solar wind: Arbitrary k , v 0 , B 0 , and $|\delta$ B |. Journal of Geophysical Research, 79(10), 1539–1541. https://doi.org/10.1029/ja079i010p01539'

[19] Hollweg, J. V. (1973). Alfvén waves in the solar wind: Wave pressure, poynting flux, and angular momentum. Journal of Geophysical Research, 78(19), 3643–3652. https://doi.org/10.1029/ja078i019p03643

[20] Usmanov, A. V., Goldstein, M. L., Besser, B. P., & Fritzer, J. M. (2000). A global MHD solar wind model with WKB Alfvén waves: Comparison with Ulysses data. In Journal of Geophysical Research: Space Physics (Vol. 105, Issue A6, pp. 12675–12695). Blackwell Publishing Ltd. https://doi.org/10.1029/1999ja000233

[21] Roberts, D. A. (1989). Interplanetary observational constraints on Alfvén wave acceleration of the solar wind. Journal of Geophysical Research: Space Physics, 94(A6), 6899–6905. https://doi.org/10.1029/ja094ia06p06899

[22] Roberts, D. A., Goldstein, M. L., & Klein, L. W. (1990). The amplitudes of interplanetary fluctuations: Stream structure, heliocentric distance, and frequency dependence. Journal of Geophysical Research, 95(A4), 4203. https://doi.org/10.1029/ja095ia04p04203

[23] Smith, E. J., Balogh, A., Neugebauer, M., & McComas, D. (1995). Ulysses observations of Alfvén waves in the southern and northern solar hemispheres. Geophysical Research Letters, 22(23), 3381–3384. https://doi.org/10.1029/95GL03268

[24] Dewar, R. L. (1970). Interaction between hydromagnetic waves and a time-dependent, inhomogeneous medium. Physics of Fluids, 13(11), 2710–2720. https://doi.org/10.1063/1.1692854

[25] Barnes, A. (1992). Theory of magnetohydrodynamic waves: The WKB Approximation revisited. Journal of Geophysical Research, 97(A8), 12105. https://doi.org/10.1029/92ja00996

[26] Stix, T. H. (1992). Waves in plasmas. American Institute of Physics.

[27] Gurevich, S. (2016). Numerical methods for complex systems I, Chapter 2 - Advection. WWU Münster, Insitute of Theoretical Physics.

[28] Hirsch, C. (1990). Numerical Computation of Internal and External Flows. vol 2., Brussels, John Wiley & Sons.

[29] Godunov, S. K. (1959). A difference method for numerical calculation of discontinuous solutions of the equations of hydrodynamics. (Russian). Mat. Sb. (N.S.), 47(89), 271–306.

[30] Boris, J. P., & Book, D. L. (1976). Flux-corrected transport. III. Minimal-error FCT algorithms. Journal of Computational Physics, 20(4), 397–431. https://doi.org/10.1016/0021-9991(76)90091-7

[31] Smolarkiewicz, P. K. (1983). A simple positive definite advection scheme with small implicit diffusion. Monthly Weather Review, 111(3), 479–486. https://doi.org/10.1175/1520-0493(1983)111<0479:ASPDAS>2.0.CO;2

[32] Kuzmin, D. (2006). On the design of general-purpose flux limiters for finite element schemes. I. Scalar convection. Journal of Computational Physics, 219(2), 513–531. https://doi.org/10.1016/j.jcp.2006.03.034

[33] Zia, H., & Simpson, G. (2019). Anti-diffusive, non-oscillatory central difference scheme (adNOC) suitable for highly nonlinear advection-dominated problems.

[34] Chin, Y. C., & Wentzel, D. G. (1972). Nonlinear dissipation of Alfvén waves. Astrophysics and Space Science, 16(3), 465–477. https://doi.org/10.1007/BF00642346

[35] Wentzel, D. G. (1974). Coronal heating by Alfvén waves. Solar Physics, 39(1), 129–140. https://doi.org/10.1007/BF00154975

[36] Vainio, R., & Spanier, F. (2005). Astrophysics Evolution of Alfvén waves by three-wave interactions in super-Alfvénic shocks. A&A, 437, 1–8. https://doi.org/10.1051/0004-6361:20042433

[37] Iroshnikov, P. S. (1964). Turbulence of a Conducting Fluid in a Strong Magnetic Field. In Soviet Astronomy, Vol. 7, p.566 (Vol. 7). https://ui.adsabs.harvard.edu/abs/1964SvA.....7..566I/abstract

[38] Kraichnan, R. H. (1965). Inertial-range spectrum of hydromagnetic turbulence. Physics of Fluids, 8(7), 1385–1387. https://doi.org/10.1063/1.1761412

[39] Verma, M. K. (1998). Mean magnetic field renormalization and Kolmogorov's energy spectrum in MHD turbulence. Physics of Plasmas, 6(5 II), 1455–1460. https://doi.org/10.1063/1.873397

[40] Vainio, R., Laitinen, T., & Fichtner, H. (2003). A simple analytical expression for the power spectrum of cascading Alfvén waves in the solar wind. Astronomy and Astrophysics, 407(2), 713–723. https://doi.org/10.1051/0004-6361:20030914

[41] Spanier, F., & Vainio, R. (2011). Three-Wave Interactions of Dispersive Plasma Waves Propagating Parallel to the Magnetic Field. Advanced Science Letters, 2(3), 337–346. https://doi.org/10.1166/asl.2009.1062

[42] Bell, A. R. (1978). The acceleration of cosmic rays in shock fronts - I. Monthly Notices of the Royal Astronomical Society, 182(2), 147–156. https://doi.org/10.1093/mnras/182.2.147

[43] Axford, W. I., Leer, E., Skadron, G., Axford, W. I., Leer, E., & Skadron, G. (1977). The Acceleration of Cosmic Rays by Shock Waves. In ICRC (Vol. 11). https://ui.adsabs.harvard.edu/abs/1977ICRC...11..132A/abstract

[44] Blandford, R. D., & Ostriker, J. P. (1978). Particle acceleration by astrophysical shocks. The Astrophysical Journal, 221, L29. https://doi.org/10.1086/182658

Appendix

Non-conservative Lax-Wendroff Scheme

Lax-Wendroff is a second order method, giving more accurate approximations of the local derivatives. The idea is to calculate the derivatives as local averages of the two neighboring cells, and comparing these to the current value of the cell. The setup for the non-conservative Lax-Wendroff scheme is the same as for the non-conservative upwind scheme, except for the calculations of the derivatives. [27]

The Lax-Wendroff scheme's evolution equation is derived again to the following form for the simulation:

$$\mathcal{I}^{\sigma}_{r,\kappa,t+\Delta t} = \left[\mathcal{I}^{\sigma}_{r,\kappa,t} - \Delta t\left(v + \frac{a}{r}\right)\frac{\partial \mathcal{I}^{\sigma}_{r,\kappa,t}}{\partial r} - \Delta t\frac{a}{r^2}\frac{\partial \mathcal{I}^{\sigma}_{r,k,t}}{\partial \kappa}\right]\exp\left(\Delta t\left(\gamma_\sigma - \frac{a}{r^2}\right)\right), \quad (59)$$

where the derivatives are defined as

$$\begin{aligned}
\frac{\partial \mathcal{I}^{\sigma}_{r_i,\kappa,t}}{\partial r} &= \frac{1}{\Delta r}(\mathcal{I}^{\sigma}_{r_{i+\frac{1}{2}},\kappa,t+\frac{1}{2}\Delta t} - \mathcal{I}^{\sigma}_{r_{i-\frac{1}{2}},\kappa,t+\frac{1}{2}\Delta t}) \\
\mathcal{I}^{\sigma}_{r_{i+\frac{1}{2}},\kappa,t+\frac{1}{2}\Delta t} &= \frac{1}{2}(\mathcal{I}^{\sigma}_{r_{i+1},\kappa,t} + \mathcal{I}^{\sigma}_{r_i,\kappa,t}) - \frac{\Delta t}{2\Delta r}\left(v + \frac{a}{r_i}\right)(\mathcal{I}^{\sigma}_{r_{i+1},\kappa,t} - \mathcal{I}^{\sigma}_{r_i,\kappa,t}) \quad (60) \\
\mathcal{I}^{\sigma}_{r_{i-\frac{1}{2}},\kappa,t+\frac{1}{2}\Delta t} &= \frac{1}{2}(\mathcal{I}^{\sigma}_{r_i,\kappa,t} + \mathcal{I}^{\sigma}_{r_{i-1},\kappa,t}) - \frac{\Delta t}{2\Delta r}\left(v + \frac{a}{r_i}\right)(\mathcal{I}^{\sigma}_{r_i,\kappa,t} - \mathcal{I}^{\sigma}_{r_{i-1},\kappa,t}) \\
\frac{\partial \mathcal{I}^{\sigma}_{r,\kappa_i,t}}{\partial \kappa} &= \frac{1}{\Delta \kappa}(\mathcal{I}^{\sigma}_{r,\kappa_{i+\frac{1}{2}},t+\frac{1}{2}\Delta t} - \mathcal{I}^{\sigma}_{r,\kappa_{i-\frac{1}{2}},t+\frac{1}{2}\Delta t}) \\
\mathcal{I}^{\sigma}_{r,\kappa_{i+\frac{1}{2}},t+\frac{1}{2}\Delta t} &= \frac{1}{2}(\mathcal{I}^{\sigma}_{r,\kappa_{i+1},t} + \mathcal{I}^{\sigma}_{r,\kappa_i,t}) - \frac{\Delta t}{2\Delta \kappa}\left(\frac{a}{r^2}\right)(\mathcal{I}^{\sigma}_{r,\kappa_{i+1},t} - \mathcal{I}^{\sigma}_{r,\kappa_i,t}) \quad (61) \\
\mathcal{I}^{\sigma}_{r,\kappa_{i-\frac{1}{2}},t+\frac{1}{2}\Delta t} &= \frac{1}{2}(\mathcal{I}^{\sigma}_{r,\kappa_i,t} + \mathcal{I}^{\sigma}_{r,\kappa_{i-1},t}) - \frac{\Delta t}{2\Delta \kappa}\left(\frac{a}{r^2}\right)(\mathcal{I}^{\sigma}_{r,\kappa_i,t} - \mathcal{I}^{\sigma}_{r,\kappa_{i-1},t}).
\end{aligned}$$

The same stability conditions apply for the Lax–Wendroff schemes as presented in section 2.2.1 (equations (25) and (24)) [27].

The results of the non-conservative Lax–Wendroff scheme can be seen in figures 32 and 33. The Lax–Wendroff method causes a sine-wave oscillation in the wave front, which can be decreased by improving the resolution of the r-axis (as can be seen if we compare this simulation with Δr of 1 $R_\odot$ to figure 10 with a Δr of 0.1 $R_\odot$). The oscillations dampen out during the simulation as can be seen in figure 33. This scheme in particular has a problem with achieving the analytical solution, so it is not capable of simulating steady-state or dynamic solutions as such, though, no investigation was conducted on the resolution's effect on the accuracy of the simulation.

LOD Upwind Scheme

Another way of implementing the evolution equation for the upwind scheme is to use a *Locally One-Dimensional* (LOD) finite-difference scheme as was done by Ng et al.

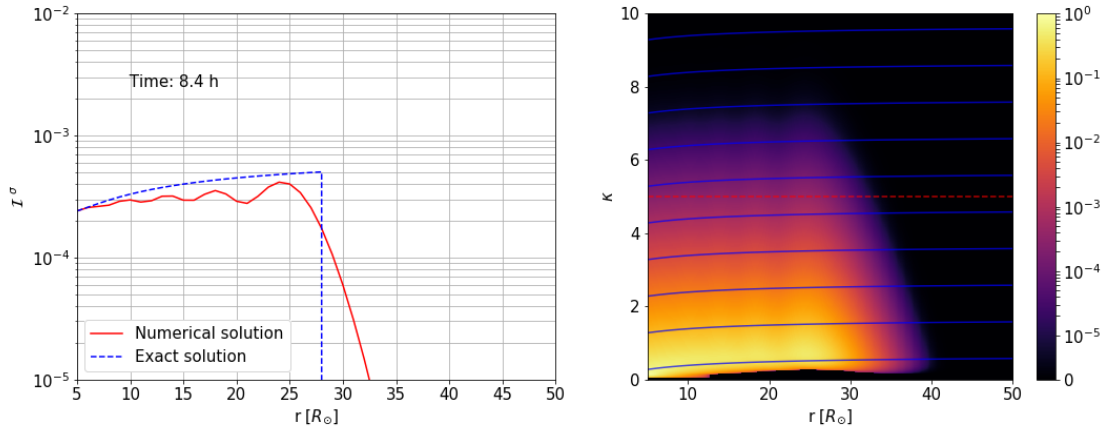

Figure 32. A non-conservative Lax–Wendroff simulation at the state where the analytical solution has reached approximately the halfway of the simulation box. The plot on the left contains a slice parallel to the r-axis denoted by the red dashed line in the plot on the right. The streamlines of the analytical solution are plotted as the blue lines on the plot on the right. The scaled intensity $\mathcal{I}^\sigma$ is denoted as a color gradient on the plot on the right. The simulation parameters used are $\Delta r = 0.5\ R_\odot$, $\Delta\kappa = 0.1$, and $\gamma = 0$

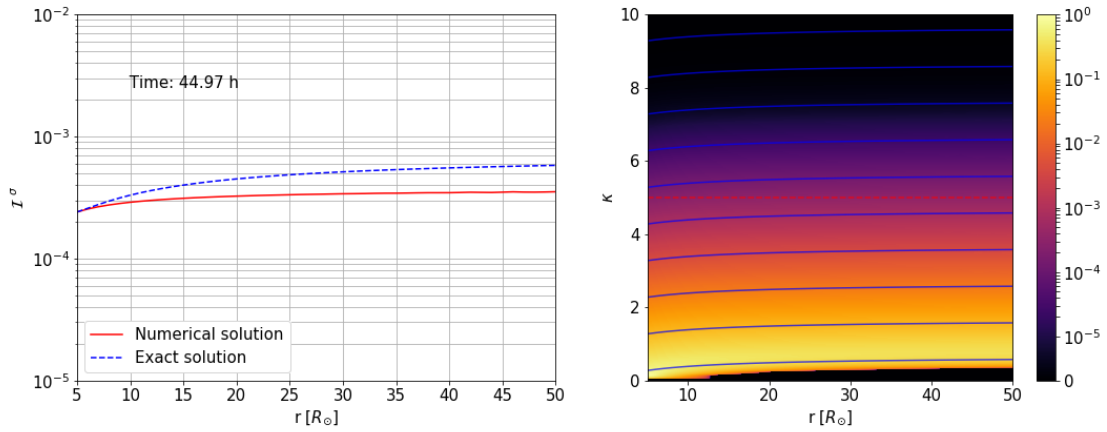

Figure 33. The steady state of the non-conservative Lax–Wendroff simulation presented in figure 32. The plot on the left contains a slice parallel to the r-axis denoted by the red dashed line in the plot on the right. The streamlines of the analytical solution are plotted as the blue lines on the plot on the right. The scaled intensity $\mathcal{I}^\sigma$ is denoted as a color gradient on the plot on the right. The simulation parameters used are $\Delta r = 0.5\ R_\odot$, $\Delta\kappa = 0.1$, and $\gamma = 0$

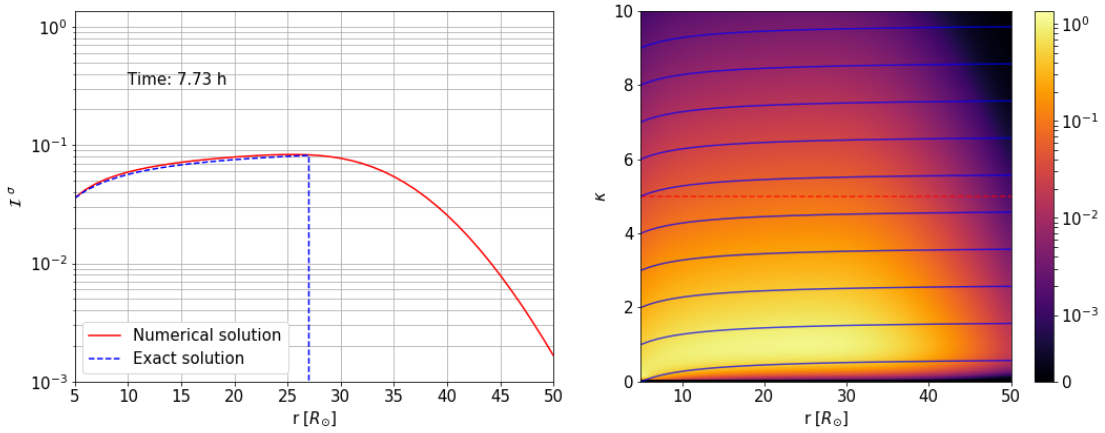

Figure 34. A non-conservative upwind simulation using the LOD implementation at the state where the analytical solution has reached approximately the halfway of the simulation box. The plot on the left contains a slice parallel to the r-axis denoted by the red dashed line in the plot on the right. The streamlines of the analytical solution are plotted as the blue lines on the plot on the right. The scaled intensity $\mathcal{I}^\sigma$ is denoted as a color gradient on the plot on the right. The simulation parameters used are $\Delta r = 0.1\ R_\odot$, $\Delta\kappa = 0.1$, and $\gamma = 0$.

[14]. The point of the LOD scheme is to break the calculation in to several simpler calculations to ease the calculation of the evolution of the waves. The wave growth is calculated implicitly and wave transport is calculated explicitly. The operations in a single time step begin from calculating the wave growth locally, followed then by the derivatives in r- and κ-directions. The equations look as follows:

$$\begin{aligned}
\mathcal{I}^\sigma_{r,\kappa,t+\frac{1}{3}\Delta t} &= \mathcal{I}^\sigma_{r,\kappa,t}\frac{1+\frac{1}{2}\Delta t\gamma_\sigma}{1-\frac{1}{2}\Delta t\gamma_\sigma} \\
\mathcal{I}^\sigma_{r,\kappa,t+\frac{2}{3}\Delta t} &= \mathcal{I}^\sigma_{r,\kappa,t+\frac{1}{3}\Delta t} - \frac{\Delta t}{\Delta r}\frac{\partial \mathcal{I}^\sigma_{r,\kappa,t+\frac{1}{3}\Delta t}}{\partial r} \\
\mathcal{I}^\sigma_{r,\kappa,t+\Delta t} &= \mathcal{I}^\sigma_{r,\kappa,t+\frac{2}{3}\Delta t} - \frac{\Delta t}{\Delta \kappa}\frac{\partial \mathcal{I}^\sigma_{r,\kappa,t+\frac{2}{3}\Delta t}}{\partial \kappa}.
\end{aligned} \tag{62}$$

where the derivatives are defined as equations (22) and (23).

The results of the LOD scheme are presented in figures 34 and 35. Looking at figure 34 we can see that the diffusion is more significant compared to the explicit upwind scheme (figure 2). LOD schemes are often paired with anti-diffusion operators to control the diffusion of the scheme. Without these operators the LOD scheme is highly inaccurate in a dynamic simulation. A slight deviation can also be detected from the analytical value in figure 35, which could be decreased by using a finer resolution, but also making the explicit upwind scheme better as a steady state solver due to the computation load.

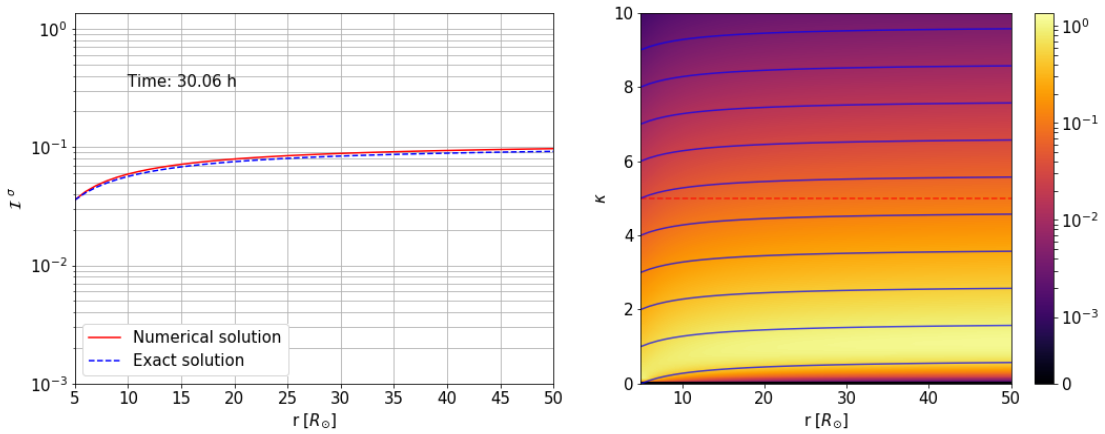

Figure 35. The steady state of the non-conservative upwind simulation presented in figure 34. The plot on the left contains a slice parallel to the r-axis denoted by the red dashed line in the plot on the right. The streamlines of the analytical solution are plotted as the blue lines on the plot on the right. The scaled intensity $\mathcal{I}^\sigma$ is denoted as a color gradient on the plot on the right. The simulation parameters used are $\Delta r = 2\ R_\odot$, $\Delta\kappa = 0.1$, and $\gamma = 0$